# A Mixed Upwind/Central WENO Scheme for the Divergence Form of the Incompressible Navier-Stokes Equations in Two-Phase Flows

# Ziyang Huang<sup>a</sup>, Guang Lin<sup>a,b,\*</sup>, Arezoo M Ardekani<sup>a,\*</sup>

<sup>a</sup> School of Mechanical Engineering, Purdue University, West Lafayette, IN 47907, USA

Abstract: In this paper, an accurate and efficient numerical scheme to solve the divergence form of the Navier-Stokes equations for two-phase flow systems is developed. The major difficulty of solving the divergence form in two-phase flows is rooted in the discontinuous nature of momentum across interfaces. To overcome this difficulty, we developed the mixed Upwind/Central WENO scheme so that no grid deformation or mapping, or explicit interface reconstruction is necessary. Our mixed Upwind/Central WENO scheme also removes the dependence on the interface tracking/capturing method so it is compatible with any popular interface tracking/capturing methods. To decouple the overall equations of the two-phase system, an efficient semi-implicit projection scheme is constructed, which shares the efficiency of pressure stabilization method while enforces divergence-free condition to machine precision, to benefit interface advection, reduction consistency as well as large density ratio. The accuracy and reduction consistency of this projection scheme are validated by numerical experiments. Several benchmark cases are performed to show the capability of the overall scheme handling realistic two-phase problems with multiple physical effects, complex interface evolution and/or large density ratio of the order of  $(\rho_{\text{water}}/\rho_{\text{air}})$ . Both quantitative and qualitative comparisons have been made and very good agreements with analytical solutions, published numerical and/or experimental results are achieved.

**Keywords**: Navier-Stokes Equations; Divergence form; Two-Phase Flow; WENO; Projection; Large Density Ratio

#### 1. Introduction

Fluid flows with interfaces, commonly referred to as two/multi-phase flow problems, have attracted much attention because of their complicated physical nature and wide-spread applications. The major difficulty of simulating these problems comes from the presence of interfaces separating different fluids. The fluid motion in bulk regions is governed by the Navier-Stokes equations, while different bulk regions are connected by boundary conditions at interfaces as those in [1], which is referred to as sharp interface representation. However, the location of the interface is not known a priori, and its evolution depends on the fluid motion, leading to a complicated non-linear system, which is challenging to theoretically analyze. Hence, numerical simulations have been widely used in studying multi-phase flow problems. The numerical method, named "one-fluid formulation" [2,3], has gained great attention, where the Navier-Stokes equations are applied in the entire computational domain while the boundary conditions connecting bulk regions are implicitly imposed, e.g., using continuous surface force (CSF) [4] or ghost fluid method [5, 6]. Under the framework of "one-fluid formulation", locations of interfaces are tracked by using the Front-Tracking method [7] or are captured by Level-Set [8], Conservative Level-Set [9, 10, 11], Volume-of-Fluid (VOF) [12] or the "THINC" method [13]. The diffusive interface representation/phase-field method [14] has also gained increasing attention, where the interface has a small but finite thickness and surface effects are modeled by chemical potential so that all the jump conditions in the sharp interface representation are regularized and smoothed across the interface. Similarly, the entire computational domain is described by

\*Corresponding authors. Email addresses: <a href="mailto:guanglin@purdue.edu">guanglin@purdue.edu</a> (G. Lin), <a href="mailto:ardekani@purdue.edu">ardekani@purdue.edu</a> (A.M. Ardekani)

<sup>&</sup>lt;sup>b</sup> Department of Mathematics, West Lafayette, IN 47907, USA

the Navier-Stokes equations, so it can be considered as a "one-fluid formulation" method. This method can be used to deal with multiphase and/or complex flow problems [15], especially for phase-change [16] and moving contact line [17], where the finite-thickness representation of interface may be more appropriate. A recent overview of comparing different interface capturing methods is proposed by Mirjalili et al. [18]. The comparisons between different models of surface tension are available in the literature, e.g. [19], where the continuous surface force and ghost fluid method are compared, and [20], where the continuous surface force and the surface stress of the phase-field method derived from chemical potential are compared. Instead of discussing different interface tracking/capturing methods or surface tension modeling, we mainly focus, in the present work, on discretizing the divergence form of the incompressible Navier-Stokes equations for two-phase flows in both time and space.

Following the "one-fluid formulation", the fluid motion is governed by the divergence form of the Navier-Stokes equations in both sharp/diffusive interface representation, with an appropriate source term.

$$\begin{cases} \nabla \cdot \boldsymbol{u} = 0, \\ \partial_t(\rho \boldsymbol{u}) + \nabla \cdot (\rho \boldsymbol{u} \otimes \boldsymbol{u}) = -\nabla p + \nabla \cdot \left[\mu (\nabla \boldsymbol{u} + \nabla \boldsymbol{u}^{\mathrm{T}})\right] + \boldsymbol{f}, \\ \rho = \rho(\boldsymbol{x}, t), \mu = \mu(\boldsymbol{x}, t), \end{cases}$$
(1.1a)
$$(1.1b)$$

$$(1.1c)$$

where u is the velocity vector, p is the pressure,  $\rho$  is the density,  $\mu$  is the viscosity, f is the body force and  $\otimes$  corresponds to the tensor product. The body force f depends on the problem considered as well as on the interface tracking/capturing method. Eq. (1.1a) is the incompressibility equation, Eq. (1.1b) represents the momentum conservation equation, and Eq. (1.1c) indicates variable material properties due to the presence of different phases. The left-hand side (LHS) of Eq. (1.1b) has different equivalent forms Eq. (1.2).

$$\partial_t(\rho \mathbf{u}) + \nabla \cdot (\rho \mathbf{u} \otimes \mathbf{u})$$
 (1.2a) is equals to

$$\rho[\partial_t \mathbf{u} + \nabla \cdot (\mathbf{u} \otimes \mathbf{u})] \tag{1.2b}$$

or

$$\rho[\partial_t \mathbf{u} + \mathbf{u} \cdot \nabla \mathbf{u}]. \tag{1.2c}$$

In single-phase problems, Eq. (1.2a) and Eq. (1.2b) are identical and are referred to as the divergence convection term while Eq. (1.2c) is referred to as the advective convection term. When the density is variable as in cases of two/multi-phase flow, only Eq. (1.2a) is referred to as the divergence convection term while we refer to Eq. (1.2b) and (1.2c) in this article as the non-divergence convection term. Mathematically, the divergence and the non-divergence convection terms Eq. (1.2) are equivalent as long as the velocity is divergence-free, which is required in Eq.(1.1a), while this is not numerically the case. The discretized non-divergence convection terms may fail to conserve the momentum. On the other hand, the momentum is discretely conserved when the divergence convection term is used since the momentum flux moving out of one cell will go into its neighboring cells. Numerical solutions of single-phase flow problems have shown in [21] that the divergence form of Navier-Stokes equations provides more physical results than the non-divergence form using the same order-of-accuracy discretization. However, the nondivergence Navier-Stokes equations are often used in two/multi-phase flow problems, even though the momentum conservation is desirable [22]. Although the "one-fluid formulation" may give an impression that the governing equations can be discretized in manners similar to those for single-phase flows, it should always be noted that material properties may be discontinuous or may experience steep transition, especially in the cases of large density/viscous ratio, which leads to additional numerical difficulty. In the case of immiscible viscous two-phase flows, no-slip and no-penetration boundary conditions are applied at the interface, resulting in a continuous velocity in the entire domain. However, the momentum can be discontinuous or can change violently across the interface because of density variation. In other words, solving the non-divergence form takes advantage of the globally continuous velocity field which is favorable for numerical practice. The process of numerically solving the divergence form in two/multiphase cases is non-trivial and is not a straightforward extension from single-phase problems since the momentum field should not be expected to be smooth anymore. This means that the numerical methods that have been successfully used in single-phase problems are probably not suitable to two/multi-phase cases although the governing equations Eq. (1.1) looks almost identical to the single-phase one.

Some efforts have been made to handle the divergence form of the Navier-Stokes equation Eq. (1.1) in two-phase problems and the significance of solving the divergence form has been gradually realized. The first scheme of this kind was proposed by Rudman [23], where the Volume-of-Fluid method was solved on a grid that was twice as fine as those for solving the Navier-Stokes equations so that the detail of the interface, as well as the density, was obtained at the faces of the velocity control volumes. Then the momentum flux was calculated, and the flux-correction method was employed to improve stability. An extension of [23] was presented by Bussmann et.al. [24], where a collocated grid was applied in order to avoid the necessity of refining the Volume-of-Fluid gird. However, viscous and surface tension effects were not considered in their numerical simulations. The significance of applying the divergence form of the Navier-Stokes equations in two/multi-phase flow problems was first discussed in [24] and further explored by Raessi and Pitsch [25], Chenadec and Pitsch [26], and Owkes and Desjardins [27]. It has been shown that more promising results are obtained by solving the divergence form when large ratios of material properties are present. Both [26] and [27] extended the geometric semi-Lagrangian method, which was originally proposed for solving the Volume-of-Fluid equation, to momentum advection. The geometric semi-Lagrangian method applied in [26] was based on [28] while the method introduced in [29], which is a flux-based scheme modified from [28], was applied in [27]. In order to improve the interface representation and consistency, [27] followed the set up in [23], where the Volume-of-Fluid gird was twice as fine as that of flow variables.

The developed schemes for the divergence form of the Navier-Stokes equations in two-phase cases mainly use the VOF method since they required an explicit representation of the interface. Although a Level Set method was used in [25], the interface reconstruction was necessary to accurately evaluate the flux density. This reconstruction process deteriorates the attraction of simplicity of the Level Set method. It should be noted that interface reconstruction is a non-trivial process in VOF method and sometimes is not straightforward to obtain it using other interface tracking/capturing methods. The geometric semi-Lagrangian method applied in [26, 27] is also very complicated, where the mapping between the fixed Eulerian grid and the deforming Lagrangian grid, and several sub-gird partitions have to be performed. As has been noticed in [24], the requirement of explicit interface representation may hinder the application of other interface tracking/capturing methods except for VOF while accurate VOF solver can be very complicated.

The difficulty of discretizing the divergence form of the Navier-Stokes equations for multiphase flow problems stems from the discontinuous nature of momentum in the sharp interface representation or from the steep variation of momentum in the diffusive interface representation. Several efforts have been made to numerically deal with discontinuity [30] and the WENO scheme [31] is considered as one of the most successful ones. The WENO schemes have been used to solve shock discontinuity in compressible flows, where the high-order accuracy is achieved while numerical oscillation is bounded (TVB). Its application to incompressible single-phase flows has also been explored in the framework of artificial compressibility [32, 33] and projection method [34, 35]. However, as far as we know, the WENO scheme has not yet been implemented for two/multi-phase Navier-Stokes equations although other technics from compressible flows such as ENO have been recommended for discretizing Eq. (1.2b, 1.2c) in two-phase flow simulations [2, 3, 7].

#### 1.1 Contributions in the present paper

In the present paper, we are proposing an accurate and efficient numerical scheme to solve the divergence form of the Navier-Stokes equations Eq. (1.1) for two-phase flows on a fixed Eulerian grid. The major difficulty comes from the discontinuous nature of momentum across interfaces. Although the kinematic and no-slip boundary conditions at the interfaces of two immiscible and viscous fluids result in continuous velocity across interfaces, the material properties of the fluids can be discontinuous across interfaces, leading to discontinuous momentum field. Compared to the previous efforts in solving this numerical challenge [23-27], our scheme has several preferable properties and advantages. We develop the mixed Upwind/Central WENO scheme to discretize the divergence convection term of momentum, which, as far as we are concerned, is the first extension of the WENO scheme to incompressible two-phase Navier-Stokes equations on a MAC grid [36]. We notice that the material property fields implicitly include the information of interface locations and the stencil candidates can sense this information, resulting in an appropriate combination of stencils following the WENO reconstruction. Because of that, our scheme does not require any explicit interface reconstruction, or grid deformation and mapping, which makes our scheme convenient to be implemented. Our mixed Upwind/Central WENO scheme, requiring information no more than distributions of material properties, also removes the dependence on the interface tracking/capturing method so it is flexible to be accompanied with any popular interface tracking/capturing methods, e.g., front tracking, level set, conservative level set, VOF, THINC or phase-field method and with different surface tension modeling. In addition, we construct a semi-implicit projection scheme, sharing the efficiency of pressure stabilization method [37-40], to decouple the two-phase system. All the discretized systems are linear with time-independent coefficient matrixes, which can be generated at the very beginning of computation without any changes during the computations. However, different from those in [37-40], our new projection scheme enforces the divergence-free condition into machine precision, which is beneficial for the advection of interface and the reduction consistency of the discretized viscous term. A similar fast pressure-correction scheme was proposed by Dodd and Ferrante [41] to decouple the two-phase Navier-Stokes equations. This scheme has successfully coupled with the mass-conserving volume of fluid scheme proposed by Baraldi et. al. [42] to study the bubbly suspension flows [43]. It splits the pressure as those in [40] to accelerate computation and obtains divergence-free velocity while treats the viscous term explicitly for applications of large Reynolds number. Although in the appendix A of [41], an implicit treatment for the viscous term was proposed, which is similar to our present work, its accuracy has not yet been explored. Specifically, the splitting error introduced by their treatment is possibly 1st-order accurate in time from Taylor expansion. In the present work, we have carefully designed the splitting error so that it is formally 2<sup>nd</sup>-order accurate in time and this has been confirmed by our numerical tests on a smooth manufactured solution. Numerical tests show that the proposed scheme is capable of dealing with complex two-phase flow phenomena, e.g. topological changes, large density ratios of the order of  $(\rho_{\text{water}}/\rho_{\text{air}})$ , and moving contact lines, accurately and efficiently.

The rest of this article is organized as follows. In section 2, we summarize the governing equations. In section 3, spatial discretization is provided and the major focus is on introducing the Upwind/Central WENO scheme for discretizing  $\nabla \cdot (\rho u \otimes u)$ , the divergence convection term. In section 4, the semi-implicit projection scheme to decouple the two-phase system is presented, followed by the discussions about its formal accuracy, efficiency, stability, and reduction consistency. In section 5, numerical simulations are performed to validate the proposed methodology. Benchmark numerical simulations are performed to show the ability of the overall scheme to deal with different two-phase problems.

# 2. Governing Equations

Following the "one-fluid formulation", the fluid motion is governed by the divergence form of the Navier-Stokes equations with the divergence convection term on the left-hand side and with appropriate initial and boundary conditions.

$$\begin{cases}
\nabla \cdot \boldsymbol{u} = 0, \\
\partial_t(\rho \boldsymbol{u}) + \nabla \cdot (\rho \boldsymbol{u} \otimes \boldsymbol{u}) = -\nabla p + \nabla \cdot \left[\mu(\nabla \boldsymbol{u} + \nabla \boldsymbol{u}^{\mathrm{T}})\right] + \boldsymbol{f}_{ext} + \boldsymbol{f}_s,
\end{cases} (2.1a)$$
(2.1b)

where u is the velocity vector, p is the pressure,  $\rho$  is the density,  $\mu$  is the viscosity,  $f_{ext}$  is the external force, e.g., gravitation  $\rho g$ ,  $f_s$  models the surface effect, e.g. surface tension, and  $\otimes$  corresponds to the tensor product. The density, viscosity and  $f_s$  are considered as the inputs of our scheme.

In order to capture the interface, the phase-field method [40, 44] is applied.

$$\partial_t \phi + \nabla \cdot (\mathbf{u}\phi) = \nabla \cdot (M\nabla \Phi), \tag{2.2a}$$

$$\Phi = \lambda [h(\phi) - \nabla^2 \phi], \tag{2.2b}$$

$$h(\phi) = \frac{1}{\eta^2}\phi(\phi^2 - 1),$$
 (2.2c)

$$\lambda = \frac{3}{2\sqrt{2}}\sigma\eta,\tag{2.2d}$$

with boundary conditions

$$\partial_n \phi = \partial_n \Phi = 0, \tag{2.2e}$$

at all the domain boundaries, where  $\phi$  is the phase-field function ranging from -1 to 1,  $\Phi$  is the chemical potential,  $\lambda$  is the mixing energy density related to surface tension  $\sigma$ , M is the mobility which is a constant,  $\eta$  determines the thickness of the interface. It should be noted that the convection term in (2.2a) is written in the conservative form by taking the advantage of the divergence-free velocity field. The material properties are linear interpolated by the phase-field function

$$\rho = \frac{\rho_1 + \rho_2}{2} + \frac{\rho_1 - \rho_2}{2} \phi , \mu = \frac{\mu_1 + \mu_2}{2} + \frac{\mu_1 - \mu_2}{2} \phi, \tag{2.2f}$$

and the momentum source  $f_s$  derived from the phase-field method to model surface tension is

$$f_{s} = \Phi \nabla \phi. \tag{2.2g}$$

We would like to emphasize that the major focus of our present study, which is developing the Mixed Upwind/Central WENO scheme to discretize the divergence convection term and constructing the efficient semi-implicit projection scheme to decouple Eq. (2.1), is independent of interface tracking/capturing method. In other words, the interface capturing method is not restricted to phase-field method Eq. (2.2). We have also used the proposed scheme in Section 3 and 4 with the Level-Set method as well. Since the discussion of the advantages and disadvantages of different interface capturing methods is outside the scope of the current work, we mainly present the results using the phase field method. For demonstration purpose, we present in Appendix C two cases, where we use our scheme to solve the divergence form of Navier-Stokes equations (2.1) while the phase-field method is replaced by the level-set method to capture interfaces and the surface tension is modeled by continuous surface force. Excellent agreements are obtained with the analytical and existing numerical solutions.

The discretization of the phase-field method is described here, and the rest of the paper will focus on discretizing the divergence convection term in space in Section 3 and on decoupling the two-phase Navier-Stokes equations in time efficiently and accurately in Section 4. The major difficulty in solving the phase-field function is the 4<sup>th</sup>-order operator. We follow the temporal discretization in [15, 40], where the 4<sup>th</sup>-order phase-field equation is separated into two independent Helmholtz equations that can be solved in sequence to obtain the solution. More detail of the temporal discretization should be referred to [15, 40]. For spatial discretization, WENOU, which is introduced in section 3 by Eq. (3.1), is applied to the

convection term and central difference is used for the Laplace operator. The balanced-force algorithm [19] is applied to  $f_s$ , where the numerical gradient operators of  $f_s$  and pressure gradient are discretized identically by central difference and they are evaluated at the same location.

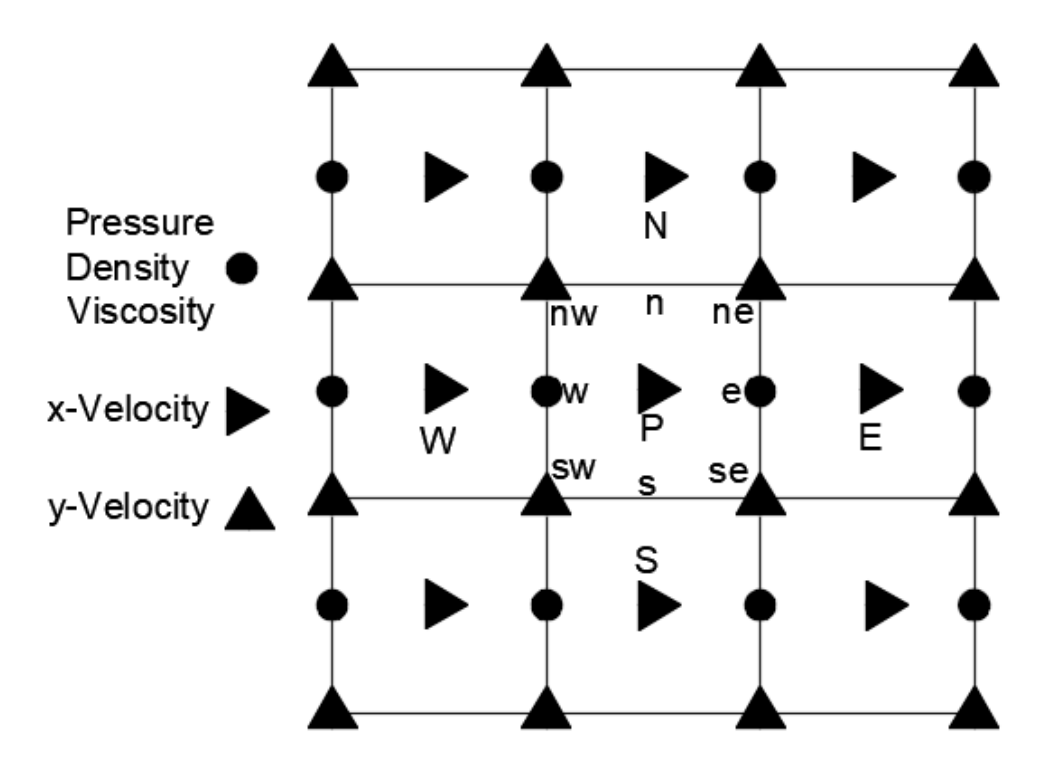


**Fig. 1** Staggered (MAC) grid arrangement and an example of u-CV.

#### 3. Spatial Discretization

We follow the staggered (MAC) grid arrangement [36] for the spatial discretization, as shown in Fig.1. This grid arrangement, which has been commonly applied in incompressible flow solvers, provides strong and compact coupling between velocity and pressure, and consequently avoid the unphysical checkboard solution of pressure that is possible in the collocated grid arrangement. The major difference from the common practice of two-phase flow simulations comes from the convection term in the left-hand side of Eq. (2.1b), which we refer to as the divergence convection term. Most attention will be paid on the discretization of this term while the other terms, e.g., the pressure gradient, and the viscous term will follow standard/common practices, e.g., in [2, 3, 45] using a central difference method. Some details of the discretization of the viscous term will be provided for the consideration of reduction consistency, followed by boundary treatments.

#### 3.1 WENO Construction

The WENO scheme was originally an up-wind type scheme [31], proposed on collocated grids for solving the conservative equations when the discontinuity is present. Later, the WENO scheme was used on a staggered grid with a central stencil and referred to as central WENO [46, 47], where it works as a non-linear interpolation method to evaluate the non-nodal values. Based on the staggered grid arrangement and the physical properties of the flow, a mixed Upwind/Central WENO scheme is proposed and applied

to discretize the divergence convection term. We follow the general procedure proposed in [31, 46, 47] to derive the necessary WENO scheme.

Given a pointwise function  $\{\varphi_i\}$  at a set of points  $\{\xi_i\}$  with equal space h, find the desired value  $\tilde{\varphi}$ 

- 1) Specify stencil candidates  $S_k$  and the whole stencil  $\bigcup_k S_k$ .
- 2) Reconstruct polynomials  $P_k$  from each stencil candidate  $S_k$  and P from the whole stencil  $\bigcup_k S_k$ .
- 3) Evaluate the values of  $\tilde{\varphi}$  with polynomials  $P_k$  and P, whose results are referred to as  $I_k$  and Q.
- 4) Determine the linear weights  $C_k$  of each stencil candidate  $S_k$  by

$$\sum_{k} C_{k} I_{k} = Q.$$

5) Determine the smoothness indicator  $IS_k$  of each stencil candidate  $S_k$  by

$$IS_k = \sum_{l} \int h^{2l-1} \left( \frac{d^l P_k}{d\xi^l} \right)^2 d\xi,$$

where l depends on the order of the polynomial  $P_k$  while the integral interval includes the location of the desired value  $\tilde{\varphi}$ .

6) Construct the non-linear weight  $\omega_k$  of each stencil candidates  $S_k$  by

$$\omega_k = \frac{\widetilde{\omega}_k}{\sum_k \widetilde{\omega}_k}$$
,  $\widetilde{\omega}_k = \frac{C_k}{(IS_k + \varepsilon^{\text{WENO}})^2}$ ,

where  $\varepsilon^{\text{WENO}}$  is a small number to avoid zero at the denominator.

7) Evaluate the desired value  $\tilde{\varphi}$  by

$$\tilde{\varphi} \approx \sum_{k} \omega_{k} I_{k}$$
.

The upwind-type WENO scheme will be referred to as WENOU while the central-type WENO scheme will be referred to as WENOC in this paper.

We follow the formula of WENOU in [31, 35].

WENOU: Given  $\{\varphi_i\}$  at  $\{\xi_i\}$  and  $\{u_{i+1/2}\}$  at  $\{\xi_{i+1/2}\}$ , approximate  $\tilde{\varphi}=\varphi\big(\xi_{i+1/2}\big)$ 

If  $u_{i+1/2} \ge 0$ ,

$$I_0 = \frac{1}{3}\varphi_i + \frac{5}{6}\varphi_{i+1} - \frac{1}{6}\varphi_{i+2},\tag{3.1a}$$

$$I_1 = -\frac{1}{6}\varphi_{i-1} + \frac{5}{6}\varphi_i + \frac{1}{3}\varphi_{i+1},\tag{3.1b}$$

$$I_2 = \frac{1}{3}\varphi_{i-2} - \frac{7}{6}\varphi_{i-1} + \frac{11}{6}\varphi_i, \tag{3.1c}$$

$$C_0 = 0.3, C_1 = 0.6, C_2 = 0.1,$$
 (3.1d)

$$IS_k = \sum_{l=1}^2 \int_{\xi_{l-1/2}}^{\xi_{l+1/2}} h^{2l-1} \left( \frac{d^l P_k}{d\xi^l} \right)^2 d\xi, \tag{3.1e}$$

else

$$I_0 = \frac{11}{6}\varphi_{i+1} - \frac{7}{6}\varphi_{i+2} + \frac{1}{3}\varphi_{i+3},\tag{3.1f}$$

$$I_1 = \frac{1}{3}\varphi_i + \frac{5}{6}\varphi_{i+1} - \frac{1}{6}\varphi_{i+2},\tag{3.1g}$$

$$I_2 = -\frac{1}{6}\varphi_{i-1} + \frac{5}{6}\varphi_i + \frac{1}{3}\varphi_{i+1},\tag{3.1h}$$

$$C_0 = 0.1, C_1 = 0.6, C_2 = 0.3,$$
 (3.1i)

$$IS_k = \sum_{l=1}^2 \int_{\xi_{l+1/2}}^{\xi_{l+3/2}} h^{2l-1} \left( \frac{d^l P_k}{d\xi^l} \right)^2 d\xi. \tag{3.1j}$$

Three WENOC schemes, which are the cornerstones of the mixed Upwind/Central WENO Scheme in section 3.2, are derived and their results are given below.

WENOC1: Given  $\{\varphi_i\}$  at  $\{\xi_i\}$ , approximate  $\tilde{\varphi} = \frac{1}{h} \int_{\xi_{i-1/2}}^{\xi_{i+1/2}} \varphi(\xi) d\xi$ 

$$I_0 = \frac{1}{24}\varphi_{i-2} - \frac{2}{24}\varphi_{i-1} + \frac{25}{24}\varphi_i, \tag{3.2a}$$

$$I_1 = \frac{1}{24}\varphi_{i-1} + \frac{22}{24}\varphi_i + \frac{1}{24}\varphi_{i+1},\tag{3.2b}$$

$$I_2 = \frac{25}{24}\varphi_i - \frac{2}{24}\varphi_{i+1} + \frac{1}{24}\varphi_{i+2},\tag{3.2c}$$

$$C_0 = -\frac{17}{240}, \ C_1 = \frac{274}{240}, C_2 = -\frac{17}{240},$$
 (3.2d)

$$IS_k = \sum_{l=1}^2 \int_{\xi_{l-1/2}}^{\xi_{l+1/2}} h^{2l-1} \left( \frac{d^l P_k}{d\xi^l} \right)^2 d\xi.$$
 (3.2e)

It should be noted that the linear weights  $C_0$  and  $C_2$  are negative, implying that it is not a convex combination of the stencil candidates, resulting in instability. After computing  $I_k$ ,  $C_k$  and  $IS_k$  from Eq. (3.2a)-(3.2e), the procedure described below has to be performed to resolve this stability issue [46]

$$\tilde{\gamma}_k^+ = \frac{1}{2}(C_k + 3|C_k|), \, \tilde{\gamma}_k^- = \tilde{\gamma}_k^+ - C_k,$$
(3.2f)

$$\sigma^{\pm} = \sum_{k} \tilde{\gamma}_{k}^{\pm}, C_{k}^{\pm} = \tilde{\gamma}_{k}^{\pm} / \sigma^{\pm}, \tag{3.2g}$$

$$\tilde{\varphi} \approx \sigma^{+} \sum_{k} \omega_{k}^{+} I_{k} - \sigma^{-} \sum_{k} \omega_{k}^{-} I_{k}, \tag{3.2h}$$

where  $\sigma^{\pm}$  and  $\omega_k^{\pm}$  are defined by the linear weights  $C_k$  from (3.2f)-(3.2g), and  $\tilde{\varphi}$ , the term being approximated, is computed from (3.2h).

WENOC2: Given  $\{\varphi_i\}$  at  $\{\xi_i\}$ , approximate  $\tilde{\varphi} = \varphi(\xi_{i+1/2})$ 

$$I_0 = \frac{1}{16}\varphi_{i-2} - \frac{5}{16}\varphi_{i-1} + \frac{15}{16}\varphi_i + \frac{5}{16}\varphi_{i+1}, \tag{3.3a}$$

$$I_1 = -\frac{1}{16}\varphi_{i-1} + \frac{9}{16}\varphi_i + \frac{9}{16}\varphi_{i+1} - \frac{1}{16}\varphi_{i+2},\tag{3.3b}$$

$$I_2 = \frac{5}{16}\varphi_i + \frac{15}{16}\varphi_{i+1} - \frac{5}{16}\varphi_{i+2} + \frac{1}{16}\varphi_{i+3},\tag{3.3c}$$

$$C_0 = \frac{3}{16}, C_1 = \frac{10}{16}, C_2 = \frac{3}{16},$$
 (3.3d)

$$IS_k = \sum_{l=1}^3 \int_{\xi_i}^{\xi_{i+1}} h^{2l-1} \left( \frac{d^l P_k}{d\xi^l} \right)^2 d\xi.$$
 (3.3e)

WENOC3: Given  $\{\varphi_i\}$  at  $\{\xi_i\}$ , approximate  $\tilde{\varphi} = \frac{1}{h} \int_{\xi_i}^{\xi_{i+1}} \varphi(\xi) d\xi$ 

$$I_0 = \frac{1}{24}\varphi_{i-2} - \frac{5}{24}\varphi_{i-1} + \frac{19}{24}\varphi_i + \frac{9}{24}\varphi_{i+1}, \tag{3.4a}$$

$$I_1 = -\frac{1}{24}\varphi_{i-1} + \frac{13}{24}\varphi_i + \frac{13}{24}\varphi_{i+1} - \frac{1}{24}\varphi_{i+2}, \tag{3.4b}$$

$$I_2 = \frac{9}{24}\varphi_i + \frac{19}{24}\varphi_{i+1} - \frac{5}{24}\varphi_{i+2} + \frac{1}{24}\varphi_{i+3}, \tag{3.4c}$$

$$C_0 = \frac{11}{60}, \ C_1 = \frac{38}{60}, \ C_2 = \frac{11}{60},$$
 (3.4d)

$$IS_k = \sum_{l=1}^3 \int_{\xi_i}^{\xi_{i+1}} h^{2l-1} \left( \frac{d^l P_k}{d\xi^l} \right)^2 d\xi, \tag{3.4e}$$

Since all the linear weights in WENOU, WENOC2 and WENOC3 schemes are positive so there is no need to use (3.2f-h) when computing them. After computing  $I_k$ ,  $C_k$  and  $IS_k$  with the formula Eq. (3.1, 3.3, 3.4), the nonlinear weights can be computed as  $\omega_k = \widetilde{\omega}_k / \sum_k \widetilde{\omega}_k$  with  $\widetilde{\omega}_k = C_k / (IS_k + \varepsilon^{\text{WENO}})^2$ . The term being approximated,  $\widetilde{\varphi}$ , is computed as  $\sum_k \omega_k I_k$ .

# 3.2 A mixed Upwind/Central WENO Scheme for the Divergence Convection Term

Using the WENOU Eq. (3.1) and WENOC Eq. (3.2-3.4), derived in the previous section, we are able to discretize the divergence convection term on a fixed Eulerian gird without any explicit interface reconstructions. We consider the integral form instead of the differential form of the divergence convection term due to the discontinuous nature of momentum at the interfaces.

$$N(\rho, \mathbf{u}) = \nabla \cdot (\rho \mathbf{u} \otimes \mathbf{u}) \approx \frac{1}{|\Omega|} \sum_{k} \int_{\partial \Omega_{k}} \mathbf{u}(\rho \mathbf{u} \cdot \mathbf{n}) \, dS \approx \frac{1}{|\Omega|} \sum_{k} \dot{m}_{k} \mathbf{u}_{k}, \tag{3.5}$$

where n is the unit outward normal of the cell faces,  $|\Omega|$  is the volume,  $\partial\Omega_k$  is the  $k^{\text{th}}$  face of the control volume  $\Omega$  and

$$\dot{m}_k = \int_{\partial \Omega_k} (\rho \mathbf{u} \cdot \mathbf{n}) \, dS \tag{3.6}$$

is the mass flux moving out from the control volume  $\Omega$  to its neighbors sharing a common face  $\partial \Omega_k$  with  $\Omega$ . In order to clearly state how to approximate the divergence convection term by the mixed Upwind/Central WENO Scheme, the discretization of the  $N_x(\rho, \boldsymbol{u})$  will be discussed in detail. The x-component of the divergence convection term is firstly approximated by Eq. (3.7).

$$N_{\chi}(\rho, \mathbf{u}) \approx \frac{\dot{m}_{\rm e} u_{\rm e} + \dot{m}_{\rm w} u_{\rm w} + \dot{m}_{\rm n} u_{\rm n} + \dot{m}_{\rm s} u_{\rm s}}{|\Omega|},\tag{3.7}$$

where e,w,n, and s represent the faces of the control volume  $\Omega$  as shown in Fig. 1 and  $\dot{m}_k$  is

$$\dot{m}_k = (\pm) \int_{\partial \Omega_k} (\rho u) \, dy, (\pm) = \begin{cases} +, k = e \\ -, k = w \end{cases}$$
 (3.8)

$$\dot{m}_k = (\pm) \int_{\partial \Omega_k} (\rho v) \, dx, (\pm) = \begin{cases} +, k = n \\ -, k = s \end{cases}$$
 (3.9)

Firstly, the velocities at the volume faces e,w,n,s have to be evaluated. Since these velocities transport the mass as well as momentum, the upwind stencil will be physically appropriate. Consequently, WENOU is applied to approximate  $u_k$  (k = e, w, s, n) with the upwind direction determined by the sign of the linear-

interpolated velocity at volume faces. Once the velocities at the volume faces have been specified, the values of  $(\rho u)$  at the volume faces e/w can be determined since the density nodes are located at the centers of those faces of the u-CV as shown in Fig. 1.

Secondly, the integral in Eq. (3.8, 3.9) has to be approximated. Instead of using the mid-point rule introduced in [2, 3, 45], WENOC1 Eq. (3.2) is applied to approximate the mass flux  $\dot{m}_k$  (k = e, w). The reason to use WENOC is twofold. First, there is no directional bias of the mass flux integration along y-direction so it is appropriate to use the central stencil. Second, in practice, the density field is regularized or smoothed close to the interface to avoid numerical difficulty caused by the discontinuous density field even in the sharp interface representation with the non-divergence convection terms. The density field implicitly includes the information of interfaces and the WENOC1 scheme is able to use this information. It also acts as a flux limiter by the nonlinear weights in the WENO scheme.

Some minor modification has to be made to approximate  $\dot{m}_k$  (k=n,s) since the density nodes and the y-velocity nodes are not collocated as shown in Fig. 1. The density is first evaluated at the cell corners ne, nw, se and, sw shown in Fig.1, where the y-velocity nodes are located, with WENOC2. Then ( $\rho v$ ) at cell corners can be evaluated. Similarly, there is no bias direction for the integral of the mass flux along x-direction so WENOC3 is applied to approximate the mass flux  $\dot{m}_k$  (k=n,s) and it is also playing a role as a flux limiter.

In summary, the procedure to approximate the divergence convection term is

Step 1: evaluate  $u_k$  (k = e, w, s, n) with WENOU

Step2: evaluate  $(\rho u)_k$  (k = e, w)

Step3: evaluate  $\int_{\partial \Omega_k} (\rho u) dy$  (k = e, w) with WENOC1

Step4: evaluate  $\rho_k$  (k = ne, nw, se, sw) with WENOC2

Step5: evaluate  $(\rho v)_k$  (k = ne, nw, se, sw)

Step6: evaluate  $\int_{\partial \Omega_k} (\rho v) dx$  (k = n, s) with WENOC3

Step7: evaluate the divergence convection term with Eq. (3.7-3.9).

A similar procedure can be used for the  $N_y(\rho, \mathbf{u})$ . Because of the staggered (MAC) grid arrangement, however, steps 1-3 are for the faces  $\partial \Omega_k$  (k = n, s) while steps 4-6 are for faces  $\partial \Omega_k$  (k = e, w).

#### 3.3 Note for Discretization of the viscous term and Boundary treatments

The viscous term has the form

$$\mathbf{D}(\mu, \mathbf{u}) = \nabla \cdot [\mu (\nabla \mathbf{u} + \nabla \mathbf{u}^{\mathrm{T}})]. \tag{3.10}$$

Its discretization follows the common choice of  $4^{th}$  or  $6^{th}$  order accurate central difference method to avoid excessive numerical error for long-time simulation. However, the high-order central difference discretization is only applied to  $\nabla \boldsymbol{u}$  while the  $2^{nd}$ -order central difference discretization is applied to  $\nabla \boldsymbol{u}^T$ . This comes from the consideration of reduction consistency. Most of the computational domain is occupied by a single fluid phase where viscosity is constant. In this case, the viscous term should numerically reduce to  $\mu \nabla^2 \boldsymbol{u}$  in most of the domain. In other words,  $\nabla \cdot (\nabla \boldsymbol{u}^T)$  has to be zero in the bulk region. To achieve this, the  $2^{nd}$ -order central difference discretization of  $\nabla \boldsymbol{u}^T$  in the MAC grid arrangement will end up with an algebraic equation the same as the discretized continuity equation Eq. (2.1a), which is enforced in each time step to zero with our projection scheme introduced in section 4. This means that with a  $2^{nd}$ -order central difference discretization,  $\nabla \cdot (\nabla \boldsymbol{u}^T)$  will be numerically zero in the bulk region, which satisfies reduction consistency. The WENO schemes require a wide stencil. Ghost points are added outside the computational domain so that we do not need to modify the stencil and/or the discretization scheme for the boundary nodes. The values of the ghost points are specified by boundary conditions. For the periodic boundary condition,

the ghost-point values are equal to the corresponding internal points. A linear interpolation has been implemented for the Dirichlet boundary condition while a central difference has been implemented for the Neumann boundary condition to specify the ghost-point values.

# 4. An Efficient Semi-Implicit Projection Method with Formally 2<sup>nd</sup>-Order Accuracy for Velocity

The projection scheme [48] is one of the most popular methods that has been widely used in single- or multi-phase flows. In the projection method, an intermediate velocity field is obtained first from the (modified) momentum equations and then based on the Helmholtz decomposition, the intermediate velocity field is decomposed into a divergence-free vector field, which is the desired velocity field, and a scalar field, which is related to pressure. The Helmholtz decomposition results in a Poisson equation. For single-phase flows, this Poisson equation has a constant coefficient while in the cases of two/multi-phase flows, a space-and time-dependent coefficient is involved. Not only solving a Poisson equation with a variable coefficient but also updating the coefficient in each time step is much more time-consuming than the one with a constant coefficient. To alleviate this issue, a method named pressure stabilization was proposed in [37-40]. In this method, the divergence-free condition is relaxed so that the divergence-free error is consistent with the time discretization error in the momentum equation. Under this relaxation, a Poisson equation with constant coefficient can be derived even in the cases of variable density. Numerical results in [38, 41] showed that minor difference was observed between the pressure-stabilization method and the one solving variable-coefficient Poisson equation.

It should be noted that a final divergence-free velocity is desirable. As mentioned in the last section, a divergence-free velocity will improve the approximation of the viscous term. More importantly, with a divergence-free velocity field, the advection equation of VOF, Level-Set and Phase-Field methods can be rewritten as a conservative equation, which is important to ensure the conservative property of the solution. Several numerical techniques can be used for the conservative equations [30, 31, 46]. In the proposed scheme, an additional step is introduced, like that in [41], to enforce the divergence-free condition.

Assuming the density and viscosity at n + 1 time level are known, we use a backward difference scheme for the sake of stability. The scheme consists of 3 steps.

Step1:

$$\frac{\gamma_0}{\Delta t} \widetilde{\boldsymbol{u}} - \nu_0 \nabla^2 \widetilde{\boldsymbol{u}} = \frac{1}{\rho^{n+1} \Delta t} \widehat{\rho} \widehat{\boldsymbol{u}} - \frac{1}{\rho^{n+1}} \boldsymbol{N}(\rho^{n+1}, \boldsymbol{u}^{*,n+1}) - \frac{1}{\rho^{n+1}} \nabla p^{*,n+1} + \frac{1}{\rho_0} \nabla (p^{*,n+1} - p^n) + \frac{1}{\rho^{n+1}} \boldsymbol{D}(\mu^{n+1}, \boldsymbol{u}^{*,n+1}) - \nu_0 \nabla^2 \boldsymbol{u}^{*,n+1} + \frac{1}{\rho^{n+1}} \boldsymbol{f}_{ext}^{n+1} + \frac{1}{\rho^{n+1}} \boldsymbol{f}_s^{n+1}, \tag{4.1}$$

Step2:

$$\begin{cases} \frac{\gamma_0}{\Delta t} (\boldsymbol{u}^{n+1} - \widetilde{\boldsymbol{u}}) = -\frac{1}{\rho_0} \nabla p', \\ \nabla \cdot \boldsymbol{u}^{n+1} = 0 \end{cases}$$
(4.2)

Step3:

$$p^{n+1} = p^n + p', (4.3)$$

where  $\gamma_0$  and  $\hat{\chi}$  depend on the time discretization scheme, e.g.,  $\gamma_0=1$ ,  $\hat{\chi}=\chi^n$  for the 1<sup>st</sup>-order and  $\gamma_0=\frac{3}{2}$ ,  $\hat{\chi}=2\chi^n-\frac{1}{2}\chi^{n-1}$  for the 2<sup>nd</sup>-order backward difference. Similarly,  $\chi^{*,n+1}$  is an extrapolation in time, e.g.,  $\chi^{*,n+1}=\chi^n$  for the 1<sup>st</sup>-order and  $\chi^{*,n+1}=2\chi^n-\chi^{n-1}$  for the 2<sup>nd</sup>-order. For the sake of stability, we follow the criteria suggested in [40] that  $\rho_0\leq \min(\rho_1,\rho_2)$  and  $\nu_0\geq \frac{1}{2}\frac{\max(\mu_1,\mu_2)}{\min(\rho_1,\rho_2)}$ . In step1, the numerical

treatment proposed in [44] and in the Appendix C of [41] to diffusion equation with variable diffusivity has been employed to the viscous term of the Navier-Stokes equations. This treatment maintains the advantage of stability while avoids a time- and space-dependent coefficient matrix resulting from the discretization. Step2 follows the pressure stabilization scheme in [37-40]. The discretization in Step2 results in a linear system of the pressure increment p', whose coefficient matrix is invariant. The pressure is updated in step3 and the velocity correction is applied so that the velocity is divergence-free (to machine precision). Except for the periodic boundary condition, we consider that  $\mathbf{n} \cdot \mathbf{u}^{n+1} = \mathbf{n} \cdot \tilde{\mathbf{u}}$  at the domain boundaries, leading to the homogeneous Neumann boundary condition for pressure correction p'.

Some properties of the proposed scheme can be analyzed by assuming the solution is smooth. The formal accuracy of a projection method is normally governed by the splitting error introduced by the decoupling of velocity and pressure. Using the Taylor expansion of step3, we can show that p' is of order  $O(\Delta t)$ , leading to  $(\mathbf{u}^{n+1} - \widetilde{\mathbf{u}}) \sim O(\Delta t)^2$ . Similarly, we can show that  $(\mathbf{u}^{n+1} - \mathbf{u}^{*,n+1})$ ,  $(\mathbf{u}^{*,n+1} - \widetilde{\mathbf{u}})$  and  $(p^{n+1} - p^{*,n+1})$  are of the order  $O(\Delta t)^2$  when 2<sup>nd</sup>-order extrapolation is applied. The analysis implies that the overall splitting error introduced to the momentum equation Eq. (2.1b) of the proposed scheme is up to 2<sup>nd</sup> order. Since that, we expect that the velocity is formally 2<sup>nd</sup>-order accurate in time when using 2<sup>nd</sup>-order backward difference and this is confirmed by our numerical test in the next section. After analyzing the formal accuracy, we consider the efficiency. The full discretization of steps 1 and 2 results in linear systems of equations for velocity u and pressure increment p'. It is clear that the coefficient matrices are timeindependent, so they can be generated and saved or even inversed at the very beginning of computation. In addition, the consequent matrices are all diagonal-dominant so that available direct or iterative linear system solvers can be efficiently applied. In each time step, there is no internal iteration (excluding the linear system solver if an iterative algorithm is applied), which is also beneficial for efficiency. Reduction consistency has also been achieved by the proposed scheme. It will reduce to the standard incremental pressure-correction scheme [48] when single-phase flow problems are considered, e.g.,  $\rho_0 = \rho_1 = \rho_2 = \rho$ and  $v_0 = \mu_1/\rho_1 = \mu_2/\rho_2 = \nu$ . It should be noted that although the spatial discretization introduced in Section 3 is based on the divergence form, splitting errors from decoupling the incompressible Navier-Stokes equations are introduced to improve efficiency, which could be non-conservative. In addition, a time integration method may also introduce non-conservative error, e.g. the backward difference is dissipative. However, the splitting errors and the time integration error in our proposed scheme are consistent with  $O(\Delta t)^2$  so that they are controllable. This has been confirmed by our numerical tests.

# 5. Validation

#### 5.1 Primary Numerical Tests

In this section, four cases are performed to validate the properties of the proposed scheme. In the first three cases, which are the Taylor-Green vortex, lid-driven cavity, and inviscid horizontal shear layer problems, we focus on the reduction consistency. The proposed scheme for two-phase flow system should recover the results of single-phase flow system when there is only one fluid. The Taylor-Green vortex is a transient problem while the lid-driven cavity is used to test the ability of the scheme to reach steady state. The inviscid horizontal shear layer tests the ability of our scheme to reach the Eulerian limit. After performing these tests, a manufacture solution will be used to evaluate the formal order of the temporal accuracy of our efficient semi-implicit projection scheme for cases with variable density/viscosity. Finally, a steady drop case is performed to clarify the effect of the viscosity ratio on the spurious current.

# A. Taylor-Green Vortex

The Taylor-Green vortex is considered as a routine test to evaluate the ability of a Navier-Stokes solver to accurately solve transient problems. When the density and viscosity are constant in the entire domain

and  $f_{ext} = f_s \equiv 0$ , we expect the proposed two-phase flow scheme, including the Mixed Upwind/Central Scheme, which discretizes the divergence convection term, and the efficient semi-implicit projection scheme, to recover the single-phase results and to reproduce the numerical properties of the standard incremental pressure-correction scheme [48]. The solution of the Taylor-Green vortex is

$$u = \sin(kx)\cos(ky)\exp(-2\mu k^2 t/\rho) \tag{5.1a}$$

$$v = -\cos(kx)\sin(ky)\exp(-2\mu k^2 t/\rho) \tag{5.1b}$$

$$p = \frac{1}{4}\rho[\cos(2kx) + \cos(2ky)]\exp(-4\mu k^2 t/\rho)$$
 (5.1c)

where k is the wave number. It is easy to check that the above expressions satisfy the Navier-Stokes equations Eq. (2.1). In this case, the domain is  $[2\pi \times 2\pi]$  with k = 1,  $\rho_1 = \rho_2 = \rho = 1$  and  $\mu_1 = \mu_2 = \mu = 0.01$ . The periodic boundary conditions are implemented at all the boundaries to all the dependent variables u, v, p.

We first fix the time step to be 0.001, while different cell sizes ranging from  $2\pi/8$  to  $2\pi/128$  are used to check the spatial order of convergence. In total 100 time steps are performed for each cell size. The numerical results are compared with the analytical solution and the maximum pointwise errors of velocity pressure, pressure gradient and divergence of velocity are listed in Table.1.

Number of cells in each direction	Error of <i>u</i> or <i>v</i>	Rate	Error of p	Rate	Error of Grad(p)	Rate	Divergence of <i>u</i>
8	1.34E-03	3.8172	0.0112	1.1926	0.069363	1.6088	3.60E-16
16	9.22E-05	5.0449	0.0049	1.2927	0.022742	2.0329	6.60E-16
32	2.79E-06	4.9520	0.002	1.8063	0.005557	1.9930	1.44E-15
64	9.03E-08	5.1051	5.72E-04	1.9481	0.001396	1.9970	2.88E-15
128	2.62E-09	-	1.48E-04	-	3.50E-04	_	5.76E-15

**Table 1**. Results of the Taylor-Green vortex 1 (time step=0.001, 100 time steps performed)

From Table1, 5<sup>th</sup>-order convergence for velocity is observed, while the pressure, as well as pressure gradient, is second-order accurate. The same convergence rates were also reported in [35], where the WENOU scheme was applied to the single-phase incompressible Navier-Stokes equation. However, this unexpected high-order convergence of velocity seems violating the numerical analysis since the second-order error from the pressure gradient will be dominant and the overall order of accuracy should be second order. Explanation of this unexpected high order was not provided in [35]. After reexamining the derivation of the solution of Taylor-Green vortex, it should be noted that the convection term is analytically balanced by the pressure gradient. Numerically, we discover that the leading orders of the convection term and of the pressure gradient cancel each other, leading to a high-order (5<sup>th</sup> order) accurate solution, which is consistent with the numerical results presented. We conclude that the high-order convergence of velocity is due to the property of the Taylor-Green vortex and the velocity is second-order accurate in space in general, limited by the approximation of the pressure gradient. Our analysis indicates that, although Taylor-Green vortex is commonly used to check the order of a Navier-Stokes solver, special attention should be paid to the obtained results.

Secondly, a fixed cell size  $2\pi/256$  is used while the time step  $\Delta t$  is changing from 0.1 to 0.00625 to obtain the temporal order of the scheme. The moment to stop the computation is at t=1 for all cases. These results are listed in Table 2 where  $L_2$  errors are computed as

$$E_{2\Delta t/\Delta t}^{L_2} = \sqrt{\sum_{i,j} \left(\alpha_{i,j}^{2\Delta t} - \alpha_{i,j}^{\Delta t}\right)^2 / (NxNy)},$$
(5.2)

where  $\alpha$  could be u, v, p, and  $N_x$  and  $N_y$  are the number of cells along x and y directions. Our observation is consistent with the mathematical proof of the standard incremental pressure-correction scheme [48] that both velocity and pressure is  $2^{\text{nd}}$ -order accurate in time under periodic boundary condition. The maximum  $|\nabla \cdot \boldsymbol{u}|$  of each  $\Delta t$  is around 2.74E-15.

Time Step $2\Delta t/\Delta t$	Error of <i>u</i> or <i>v</i>	Rate	Error of p	Rate
0.1/0.05	1.09E-06	2.0011	3.47E-06	2.0014
0.05/0.025	2.73E-07	2.0006	8.66E-07	2.0007
0.025/0.0125	6.83E-08	2.0003	2.16E-07	2.0003
0.0125/0.00625	1.71E-08	-	5.41E-08	-

**Table 2.** Results of the Taylor-Green vortex 2 (cell size= $2\pi/256$ , end time=1)

#### B. Lid-Driven Cavity

The lid-driven cavity flow is another case that is used to evaluate the reduction consistency of the proposed scheme and further test its ability to accurately reach the steady state. There is no analytical solution for this case, while standard numerical results are available in [49]. It has been shown that complicated flow patterns can be generated in such a simple geometry and setup when Reynolds number Re increases. We follow the standard setup that the domain is  $[1 \times 1]$  with  $\rho_1 = \rho_2 = \rho = 1$  and  $\mu_1 = \mu_2 = \mu = 1/Re$ . All boundaries are no-slip and no-penetration. The upper wall is moving horizontally with a velocity equal to unity, while the other walls are stationary. We perform three cases of Reynolds numbers 100, 1,000 and 3,200. For the cases of Reynolds number 100 and 1,000, the domain is discretized by  $50 \times 50$  cells with time step 0.01, while  $100 \times 100$  cells are used in the case of Re=3,200 to capture the small-scale motion near the cavity corners with time step 0.005. 1,000, 5,000 and 30,000 time steps are performed in these three cases, respectively. Our results of u-velocity at the vertical centerline and v-velocity at the horizontal centerline are compared with the corresponding data in [49] and shown in Fig. 2. Very good agreement is achieved in all three cases with Reynolds numbers 100, 1000 and 3200. The streamlines of these three cases are also presented in Fig. 3 which are also in agreement with those in [49].

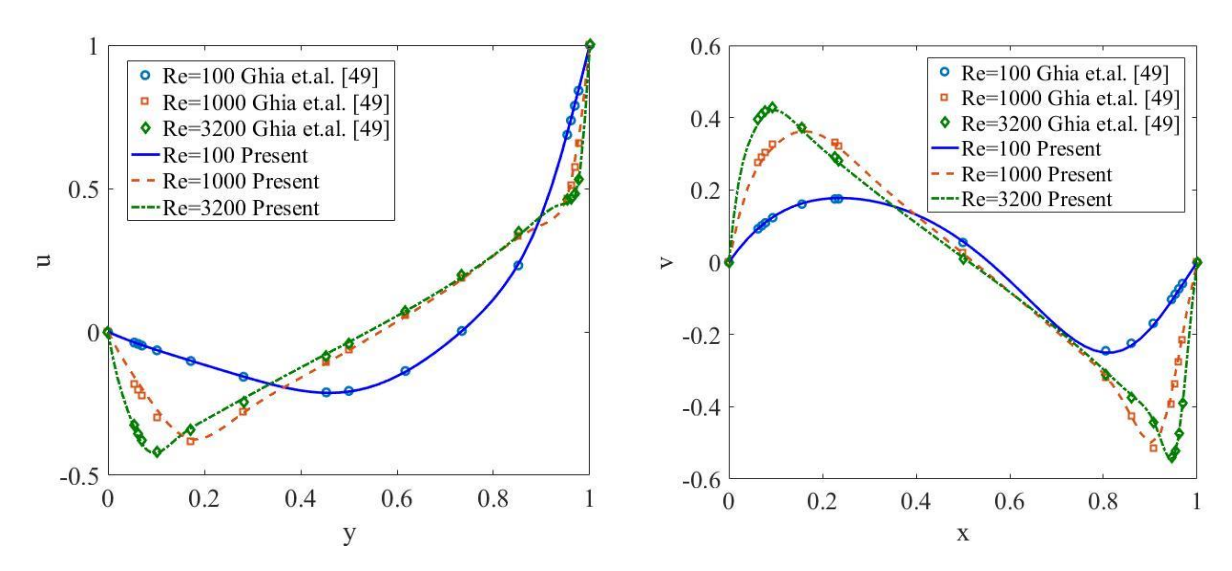


**Fig.2** Numerical results of the driven cavity. Left u-velocity at the vertical centerline. Right: v-velocity at the horizontal centerline. Ghia et.al.'s results [49] Circle: *Re*=100, Square: *Re*=1000, Diamond: *Re*=3200. Present Solid line: Re=1000, Dash line: Re=1000, Dash-Dot line: Re=3200.

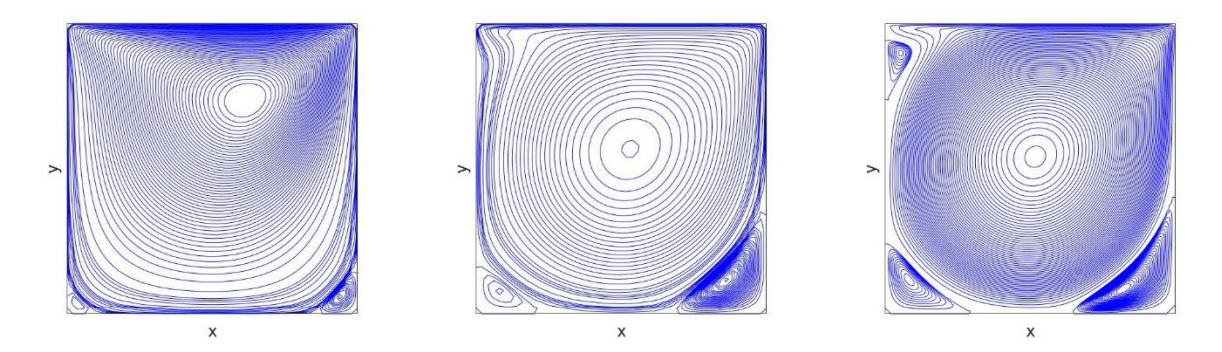


Fig. 3 Streamlines of the driven cavity. Left: Re=100, Middle: Re=1,000, Right: Re=3,200

#### C. Inviscid horizontal shear layer

The inviscid horizontal shear layer problem from Bell et.al. [50] is performed to test the ability of the present scheme to deal with the Eulerian limit. We followed the problem set up in [50], where the computational domain is  $[1 \times 1]$ , with  $\rho_1 = \rho_2 = 1$ ,  $\mu_1 = \mu_2 = 0$ . The double periodic boundary condition is applied. 128 and 256 cells along each direction were used and the time step  $\Delta t$  was  $10^{-3}$ . The initial condition was

$$u = \begin{cases} \tanh\left(\frac{y - 0.25}{\delta_1}\right), \text{ for } y \le 0.5\\ \tanh\left(\frac{0.75 - y}{\delta_1}\right), \text{ for } y > 0.5 \end{cases}, v = \delta_2 \sin(2\pi x)$$

$$(5.3)$$

with  $\delta_1 = 1/30$  and  $\delta_2 = 0.05$ . The vorticity ( $\omega = \nabla \times u$ ) contours from  $256 \times 256$  cells are shown in Fig. 4 and excellent agreements with those in [50] was achieved. It is worth noting that although  $256 \times 256$  cells are used, our result preserves very fine vortex structure which only appears with  $512 \times 512$  cells in [50]. This means that our scheme is more accurate and is able to resolve smaller structure with the same grid resolution.

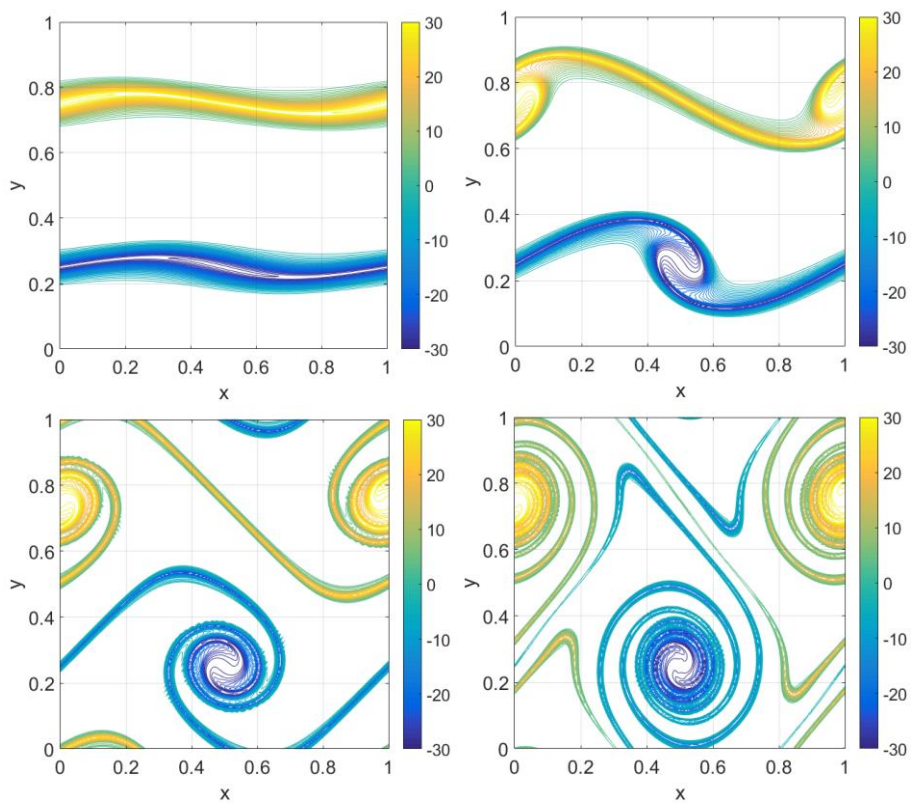


Fig.4 Vorticity contour with 256 × 256 cells. From left to right, top to bottom, time=0.4, 0.8, 1.2, 1.8.

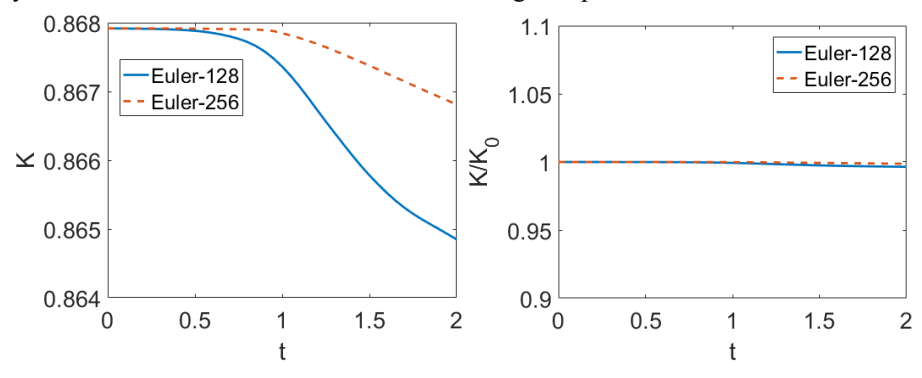


Fig.5 Kinetic energy versus time with  $128 \times 128$  and  $256 \times 256$  cells.

The kinetic energies  $K = \int_{\Omega} (u^2 + v^2) d\Omega$  from both the 128 × 128 and the 256 × 256 cells are shown in Fig. 5. For a Eulerian flow, the kinetic energy K is conserved since there is no viscous dissipation. However, numerical dissipation from time and/or space discretization will introduce kinetic energy loss. Our numerical results show that the kinetic energy maintains its initial value for a while and then begins to decay. When we refine the grid, we have a longer period of constant kinetic energy and a slower decaying rate. The overall kinetic energy loss is about 0.3% and 0.1% for 128 × 128 and 256 × 256 cells, respectively.

#### D. Manufactured solution for variable density/viscosity fields

Here, we evaluate whether the overall scheme works properly when density and viscosity fields are changing in both time and space. In addition, the analysis that the splitting error introduced to the momentum equation is consistent with the time discretization up to formally 2<sup>nd</sup>-order has to be validated. A manufactured solution with variable density and viscosity fields is constructed. We assume the velocity, pressure, density as well as viscosity are smooth and have the forms

$$u = \sin(\pi x)\cos(\pi y)\sin(t) \tag{5.4a}$$

$$v = -\cos(\pi x)\sin(\pi y)\sin(t) \tag{5.4b}$$

$$p = \sin(\pi x)\sin(\pi y)\cos(t) \tag{5.4c}$$

$$\phi = \cos(\pi x)\cos(\pi y)\sin(t) \tag{5.4d}$$

$$\rho = \frac{\rho_1 + \rho_2}{2} + \frac{\rho_1 - \rho_2}{2} \phi, \, \mu = \frac{\mu_1 + \mu_2}{2} + \frac{\mu_1 - \mu_2}{2} \phi \tag{5.4e}$$

An appropriate source term f derived from the manufactured solution is added to the Navier-Stokes equation. The constructed velocity satisfies with the continuity equation. In this case, the density and viscosity are time- and space-dependent. Our focus is on the formal order of the splitting error for the velocity field. The density as well as viscosity fields is given based on Eq. (5.4d-e) in each time step and then the proposed scheme is performed. However, practically we are unable to isolate the splitting error from the overall temporal error, which consists of the splitting error and time discretization error. Since a  $2^{nd}$ -order backward difference scheme is applied in time discretization, we expect at least  $2^{nd}$ -order of convergence for the splitting error if the observed overall temporal error is also  $2^{nd}$ -order for velocity.

The computational domain is  $[2 \times 2]$  and is discretized using 256 cells in each direction to eliminate spatial error with a sufficient number of cells. The density and viscosity are  $\rho_1 = 100$ ,  $\rho_2 = 1$ ,  $\mu_1 = 1$   $\mu_2 = 0.01$ . The time step  $\Delta t$  is ranging from 0.1-0.00625 and the computation is stopped at t = 1. The symmetry boundary conditions are imposed at all the domain boundaries. The  $L_2$  errors Eq. (5.2) of velocity components and pressure obtained using different time steps are listed in Table 3. We observe that the overall temporal errors of velocity components converge with the rate  $O(\Delta t)^2$  which is the same as the formal order of the time discretization, implying also the  $2^{\rm nd}$ -order convergence of the splitting error. Our observation is consistent with our analysis of the present scheme in section 4. The error of pressure is consistent, and we can expect formally better than  $1^{\rm st}$ -order accurate in time with small time step. The maximum  $|\nabla \cdot u|$  of each  $\Delta t$  is around 6.46E-15. In two-phase flow problems, which are often transient, the time step is usually small in practice in order to capture the dependence of physics on time, implying that the formally  $2^{\rm nd}$ -order splitting error can be very small. As shown in [38], even the formally  $1^{\rm st}$ -order splitting error introduced by pressure-stabilization scheme makes little difference to the solution.

These numerical results show that no matter what the cell size or time step is, the present projection scheme enforces the divergence-free condition accurately to machine precision, like that in [41], with both invariable and variable material properties. This property was not achievable in [37-40] while the present scheme shares the same efficiency as those in [37-40], which has been discussed in section 4. In addition, the mixed Upwind/Central WENO scheme, which discretized the divergence convection term, works accurately for variable density/viscosity fields.

It should be noted that, so far, all the numerical tests are unrelated to any interface tracking/capturing methods. In other words, all the properties shown by the numerical experiments belong to the proposed scheme solving the divergence form of the Navier-Stokes equations and they are independent of interface tracking/capturing methods. It should again be noted that, so far, the accuracy discussed and tested is the

formal accuracy, which is defined for a smooth solution. For real two-phase flows, the order of accuracy depends not only on the Navier-Stokes solver but also on the interface tracking/capturing methods. Generally speaking, the two-phase flow solution is not smooth, and the accuracy would probably be less than the formal accuracy.

Time Step $2\Delta t/\Delta t$	Error of <i>u</i>	Rate	Error of <i>v</i>	Rate	Error of p	Rate
0.1/0.05	1.86E-03	1.2543	1.30E-03	1.0659	9.04E-02	0.0715
0.05/0.025	7.82E-04	1.9959	6.22E-04	2.0015	8.60E-02	3.2521
0.025/0.0125	1.96E-04	2.1622	1.55E-04	2.1895	9.03E-03	1.6870
0.0125/0.00625	4.38E-05	-	3.40E-05	-	2.80E-03	-

**Table 3.** Results of the manufactured solution (cell size=2/256, end time=1)

## E. Steady drop

Although the velocity in the two-phase flows is continuous across the interface, the derivatives of the velocity can be discontinuous since the shear stresses from different fluid phases have to be balanced at the interface. In other words, whenever there is viscosity difference between the two fluids, there is always discontinuous velocity derivatives and this discontinuity is stronger for larger viscosity ratios. This can lead to large errors in the computation of the divergence of the velocity, which provides the source of error for the pressure equation Eq. (4.2), and, as a result, leads to unphysical spurious current. To clarify this effect, the steady drop case is considered. In this case, the phase-field equation Eq. (2.2) is solved.

A drop of radius R=2 is located at the center of an  $8 \times 8$  domain. Free slip boundary conditions were applied at all the boundaries. All the velocity components and pressure are set to be zero initially. Since the drop is in its equilibrium shape, the velocity components should maintain zero and there should be no displacement and deformation of the drop. All the cases have a unity density ratio, with the fixed surface tension 730, and fixed cell size R/20, so that the circle is well-resolved, and time step is  $\Delta t = 10^{-6}$ .

The inviscid case was performed to be the reference case, where both fluids inside and outside the drop have the same density and are inviscid. The only driving force is the numerical error introduced by the imbalance between the pressure and the surface force  $f_S$  from the phase-field method. In addition, cases with different viscous ratios  $\mu_1/\mu_2$ , where  $\mu_1$  is the viscosity of the fluid inside the drop while  $\mu_2$  is the one outside, ranging from  $10^{-3}$  to  $10^3$ , were performed and compared to the inviscid case. Both the  $L_2$  and  $L_\infty$  norms of the x-component velocity u after 1 and 1000 time steps are summarized to represent the strength of the spurious current in Table 4.

From Table 4, the strength of the spurious currents is very small in all the cases. The strengths of the spurious currents for high viscosity ratio cases are similar to the inviscid one. It is clear that, by using the proposed scheme, the strength of the spurious current is unrelated to whether the fluid inside the drop is more viscous than the one outside or not, or to the ratios of the viscosity of the fluids. In addition, the strength of the spurious current after 1000 time steps is 1000 times larger than those after 1 time step, implying a linear growth of the spurious current. In other words, the growing rate of the spurious current does not increase during the computation. In conclusion, with our scheme, the viscous ratio doesn't magnify the unphysical spurious currents.

**Table4.** The  $L_2$  and  $L_{\infty}$  norms of the velocity u of the steady drop case with different viscosity ratios

u lu -notio	After 1 T	ime Step	After 1000 Time Steps		
$\mu_1/\mu_2$ =ratio	$L_2$	$L_{\infty}$	$L_2$	$L_{\infty}$	
0/0	8.87E-07	7.36E-06	8.87E-04	7.36E-03	
$10^{-3}/10^{-3} = 1$	8.87E-07	7.36E-06	8.87E-04	7.36E-03	
$10^{-3}/10^{-2} = 10^{-1}$	8.87E-07	7.36E-06	8.87E-04	7.35E-03	
$10^{-3}/10^{-1} = 10^{-2}$	8.87E-07	7.36E-06	8.84E-04	7.34E-03	
$10^{-3}/1 = 10^{-3}$	8.87E-07	7.36E-06	8.62E-04	7.20E-03	
$10^{-2}/10^{-3} = 10$	8.87E-07	7.36E-06	8.87E-04	7.35E-03	
$10^{-1}/10^{-3} = 10^2$	8.87E-07	7.36E-06	8.84E-04	7.33E-03	
$1/10^{-3} = 10^3$	8.87E-07	7.36E-06	8.62E-04	7.08E-03	

# 5.2 Two-phase flow Tests

The properties of our scheme including reduction consistency, formal accuracy, and the effect of viscosity ratio on spurious current have been tested with primary numerical tests in section 5.1 and all the results are accurate and consistent with the numerical analysis. The following four cases are the benchmark two-phase flow problems, showing that the proposed mixed Upwind/Central WENO Scheme, discretizing the divergence convection term, and the efficient semi-implicit projection scheme, decoupling the two-phase Navier-Stokes equations, are able to handle real-world two-phase flow problems. The convergence behavior of the present scheme coupled with the phase-field method in real-world two-phase problems will be discussed by using the capillary waves, whose exact solutions are available. It is the interface capturing method that is responsible to maintain mass conservation. The phase-field method shows very good mass-conservation property in all the following cases. The results of the mass changes in each case are reported in Appendix A.

## F. Capillary Waves

A slightly perturbed horizontal interface separating the heavier fluid 2 at the bottom and the lighter fluid 1 at the top will induce an interfacial capillary wave that is gradually attenuated due to viscosity. The exact sharp interface solution is available by Prosperetti [52] using a perturbation analysis. In this case, we are going to analysis the convergence behavior of the proposed scheme coupled with the phase-field method. Although the formal accuracy of the scheme has been tested in section 5.1 with smooth solutions, there are jumps in real-world two-phase solutions, which will deteriorate the accuracy.

Following the set up in [51], the domain is  $[2\pi \times 2\pi]$  with surface tension 2. The initial perturbation is modeled by a sinusoidal wave with amplitude  $A = 0.01 \times 2\pi$  and wavelength k = 1. The x direction is discretized by 33 cells, which is sufficient to resolve a wave with wavelength 1. The odd number of cells in the x direction is assigned so that there are nodal points located at the center of the domain. The free slip boundary condition is implemented at the top and bottom boundaries while the symmetry boundary condition is implemented at the left and right boundaries. We consider the number of cells in the y direction to be 17, 33, 65, 129, 257 cells, the density and viscosity ratio to be 1,10,100 with kinematic viscosity 0.0647, and the interface thickness  $\eta = 3\Delta y$ ,  $4.5\Delta y$ ,  $7\Delta y$ ,  $10\Delta y$ . The numerical results are compared with the analytical result. The  $L_2$  errors of all the cases are shown in Fig.6.

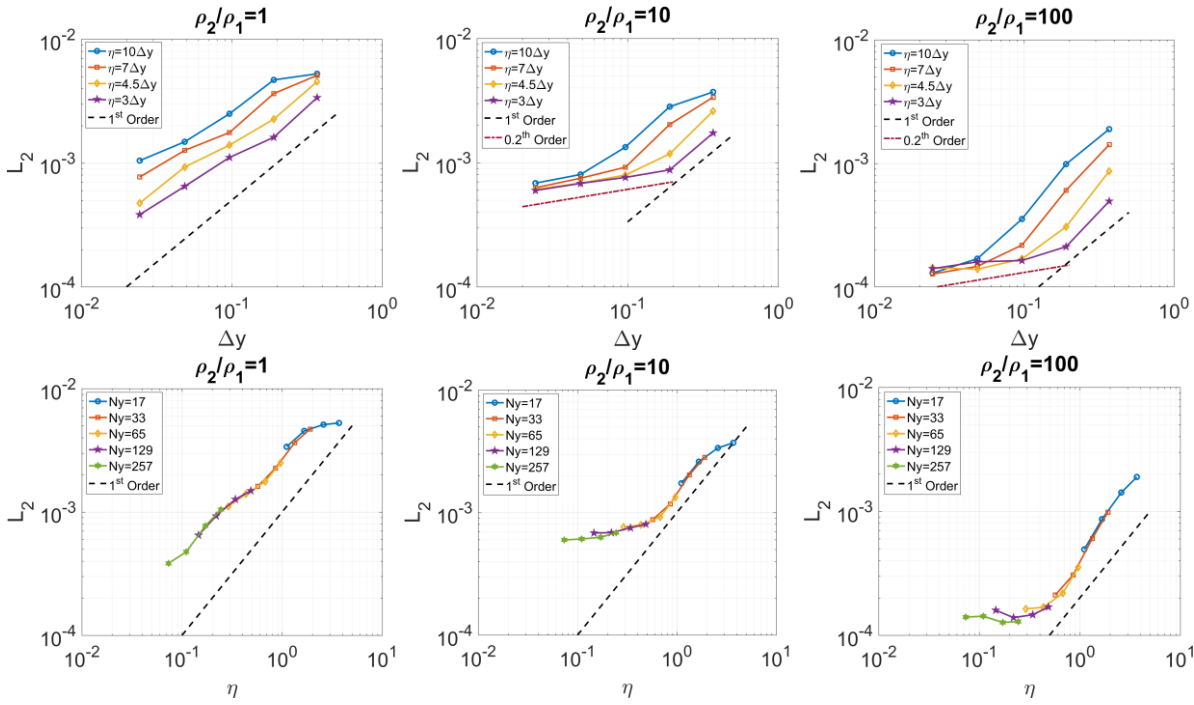


Fig. 6  $L_2$  errors of the capillary wave cases. Left column:  $\rho_2/\rho_1 = 1$ ; Middle column:  $\rho_2/\rho_1 = 10$ ; Right column  $\rho_2/\rho_1 = 100$ ; Top row: errors with respect to  $\Delta y$ ; Bottom row: errors with respect to  $\eta$ 

It is clear that the numerical error is consistent such that the error decreases when the cell size or interface thickness is reduced. When refining the cell size, the truncation error from the discretization of the continuous governing equations is getting smaller. When reducing the interface thickness, the model error from approximating the sharp interface solution with a diffuse interface model (the phase-field method) is also reduced. In general, we observe that the order of accuracy with respect to cell size is close to but less than 1st-order accurate while the order of accuracy with respect to interface thickness is about 1st-order accurate. However, we also observe that the convergence rate slows down after some cell sizes and even a little bit increases with smaller interface thickness. These behaviors of convergence imply that the truncation error and the model error is not the complete picture of the errors in a phase-field system. Jacqmin [53] had a detailed description of the phase-field dynamics in two-phase flows and analyzed different kinds of errors in the phase-field system. Jacqmin [53] shows that the truncation error is always less than 1st-order and the model error is 1st-order with respect to interface thickness. Jacqmin [53] also shows that there are other errors, called intrinsic errors in this paper, from the modification of the intrinsic energy balance of the phase-field system by discretized representation and transportation of the phase-field system. These intrinsic errors, although small, growth with respect to  $(\eta/h)$ , where h is the cell size and specifically is  $\Delta y$  in this case. When the cell size and/or  $(\eta/h)$  is large, the truncation error and the model error are dominant, and the numerical error converges with the correct order. When the cell size and/or  $(\eta/h)$  gets smaller, the truncation error and the model error become smaller and smaller, and the intrinsic errors begin to appear, which slows down the convergence rate. When  $(\eta/h)$  continues decreasing, inconsistency can appear such that the error with respect to smaller  $(\eta/h)$  is larger than that with larger  $(\eta/h)$  since the intrinsic errors increase as  $(\eta/h)$  decreases. We also discovered, from our numerical results, that the intrinsic errors increase also with respect to density ratio. In the range of cell sizes and  $(\eta/h)$  considered in the numerical tests, the numerical error in the matched density case is still in the regime where the truncation error and the model error are dominant and both of them converge with the correct rate. The second regime where the intrinsic errors begin to appear and slow down the convergence rate occurs in the case of

 $(\rho_2/\rho_1=10)$ . The third regime where the intrinsic error becomes dominant and inconsistency with respect to  $(\eta/h)$  appears occurs in the case of  $(\rho_2/\rho_1=100)$ . In other words, the density ratio tends to signify the intrinsic errors of the phase-field system, which has not been discussed by Jacqmin [53]. In order to show that there are intrinsic errors in the matched density case, we perform computations with a wider range of  $(\eta/h)$  and with 513 cells along the y direction. With a finer grid, the truncation error and the model error are smaller, and it is easier to show the intrinsic errors. We do observe in Fig. 7 the inconsistent regime after  $\eta < 4.5\Delta y$  and the interface almost doesn't move in the case of  $\eta = \Delta y$ . This weird result of "trapped" interface actually has been emphasized by Jacqmin [53]. Based on the analysis in [53], when an interface moves across a cell, there is an interfacial energy flucturation. In other words, there is an energy barrier to be overcome before the interface can move across a cell. This energy barrier, which is a kind of intrinsic errors, increases when  $(\eta/h)$  decreases. If this energy barrier is so large that it is unable to be overcome by the driven force of the two-phase flow, the interface won't move, and this is the case when  $\eta = \Delta y$ . So far, all the numerical results are fully consistent with phase-field dynamics and its error analysis. Interested readers can study Jacqmin [53] for more detailed descriptions and discussions about the phase-field dynamics and its error analysis.

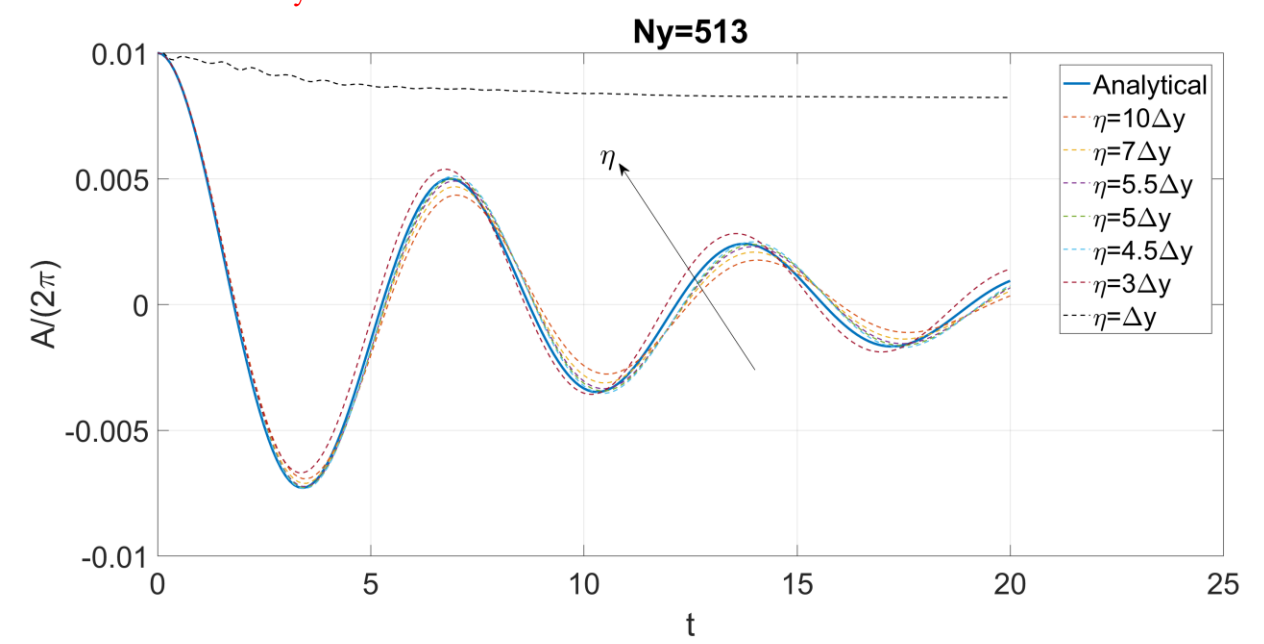


Fig. 7 Capillary waves obtained from different  $\eta$  with  $\Delta y = 2\pi/513$  and  $\rho_2/\rho_1 = 1$ 

To illustrate the flexibility of our scheme, we have performed the matched density case with the Level-Set method and the continuous surface force as well. Excellent agreement with the analytical solution is obtained. The Level-Set results are in Appendix C.

#### G. Rayleigh-Taylor Instability

The second case is the Rayleigh-Taylor instability, which is considered as a benchmark problem for two-phase flows and is important to capture the motion of miscible fluids. The physical configuration of Rayleigh-Taylor instability involves the complicated evolution of the interface. A denser fluid is initially staying above a lighter fluid with a horizontal interface separating these two fluids. When a perturbation is applied, the interface is unconditionally unstable, and these two fluids penetrate each other. During the penetration, small-scale flow patterns appear, generating complicated interfaces between these fluids. We consider two Atwood numbers  $At = (\rho_{\text{max}} - \rho_{\text{min}})/(\rho_{\text{max}} + \rho_{\text{min}})$  and compare our results with those by Ding et. al. [54], by Guermond et.al. [55] and by Tryggvason [56] for the case of At = 0.5 and by Zhao et.

al. [57] for the case of At = 0.2. The general setup is that the domain is  $[0.5L \times 4L]$  with the no-slip/penetration boundary conditions at the top and the bottom boundaries while the symmetric boundary condition is imposed at the two lateral boundaries. The domain is discretized using  $64 \times 512$  cells with  $\eta = 1.28\Delta y = 0.01$ .

In the case of Atwood number 0.5, the governing equation is nondimensionalized by the length scale L, the density scale  $\rho_2$  and the velocity scale  $\sqrt{gL}$ . The density ratio is 3 and the viscosity is chosen in such a way that the Reynolds number based on the length, density, velocity, and viscosity scales is 1000. The initial horizontal perturbation is modelled by a sinusoidal wave at y = 2L with an amplitude 0.1L and wavelength  $2\pi$ . Quantitative comparison can be achieved by measuring the transient locations of the tips of bubbles going up and down as shown in Fig. 8.

We observe a very good agreement between our results and those in [54-56]. Since the flow considered by Tryggvason [56] is inviscid, the minor discrepancy is present. However, the difference between our results and those in [54, 55] is indistinguishable since the same set up is used. The flow patterns at different times are compared against those in [54] in Fig. 9. Again, a very good agreement for the interface structure and temporal evolution is achieved. From Fig.8, the denser fluid is initially going down while the lighter one is going up. A small-scale perturbation appears and begins to grow at the lateral side of the falling column of the denser fluid, resulting in a mushroom-like shape of the interface. The tip of this growing perturbation then rolls up into the region of the lighter fluid and forms a long and thin tail. As time goes on, the tail becomes so thin that topological change appears, resulting in small structure patterns.

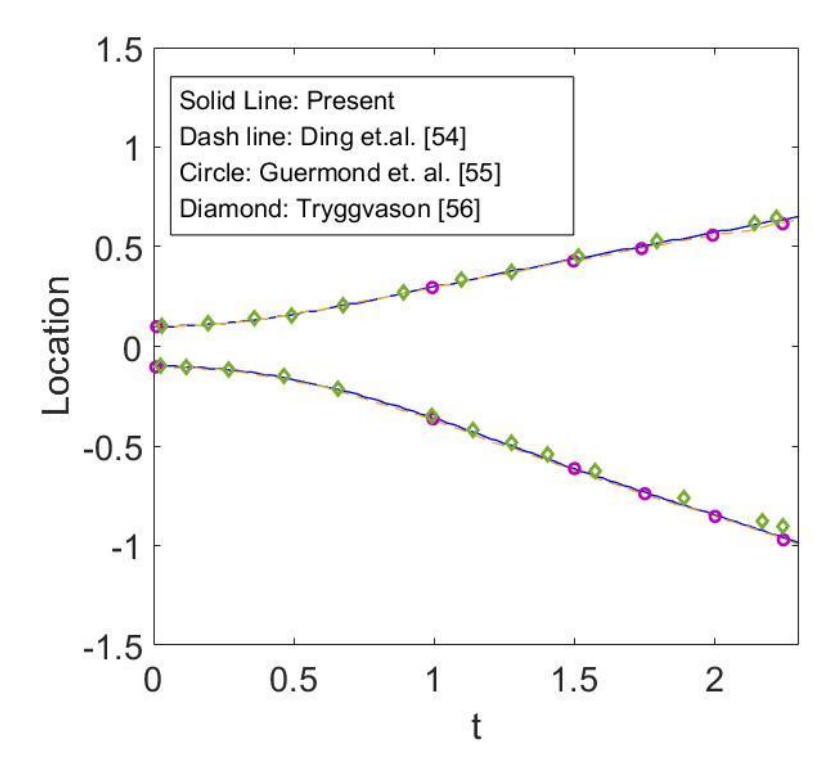


**Fig. 8** The transient locations of the tips of bubbles going up and down when *At*=0.5. Solid line: Present, Dash line: Ding et.al. [54], Circle: Guermond et. al. [55], Diamond: Tryggvason [56].

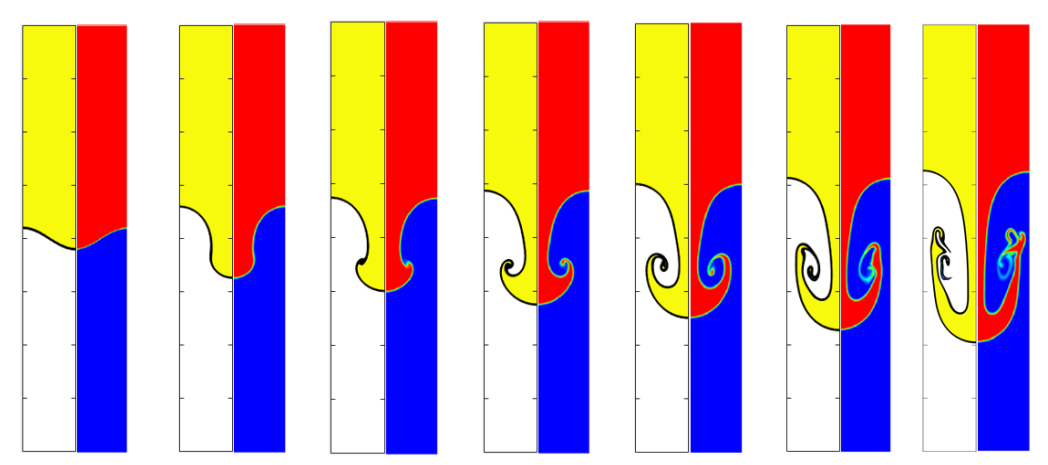


**Fig. 9** Flow patterns of the Rayleigh-Taylor instability with *At*=0.5 at *t*=0, 1, 1.25, 1.5, 1.75, 2, 2.25. Left Panels (yellow and white): Present, Right Panels (Blue and Red): Ding et. al. [54]. Yellow and Red: Denser fluid; White and Blue: Lighter fluid

The case of Atwood number 0.2 involves more complex interfacial movements. We follow the set up in [57], where  $\rho_1 = 1.5$ ,  $\rho_2 = 1$ ,  $\mu_1 = 0.00195$ ,  $\mu_2 = 0.0013$  and L = 1. The same initial perturbation as those in the case Atwood number 0.5 is employed except that the amplitude is 0.05. The corresponding snapshots at different moments are presented in Fig. 10. Our results are in agreement with those in [57]. Similar physical phenomena are observed except that more violent topological changes occur, e.g., bubble pinch-off.

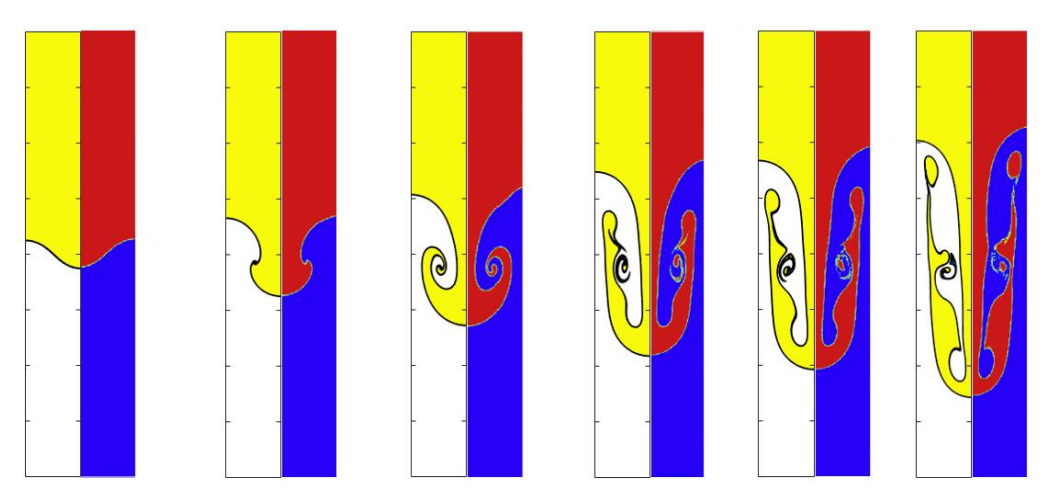


**Fig. 10** Flow patterns of the Rayleigh-Taylor instability with At=0.2 at t=0.5, 1.0, 1.5, 2.0, 2.2, 2.5. Left Panels (yellow and white): Present, Right Panels (Blue and Red): Zhao et. al. [57]. Yellow and Red: Denser fluid; White and Blue: Lighter fluid

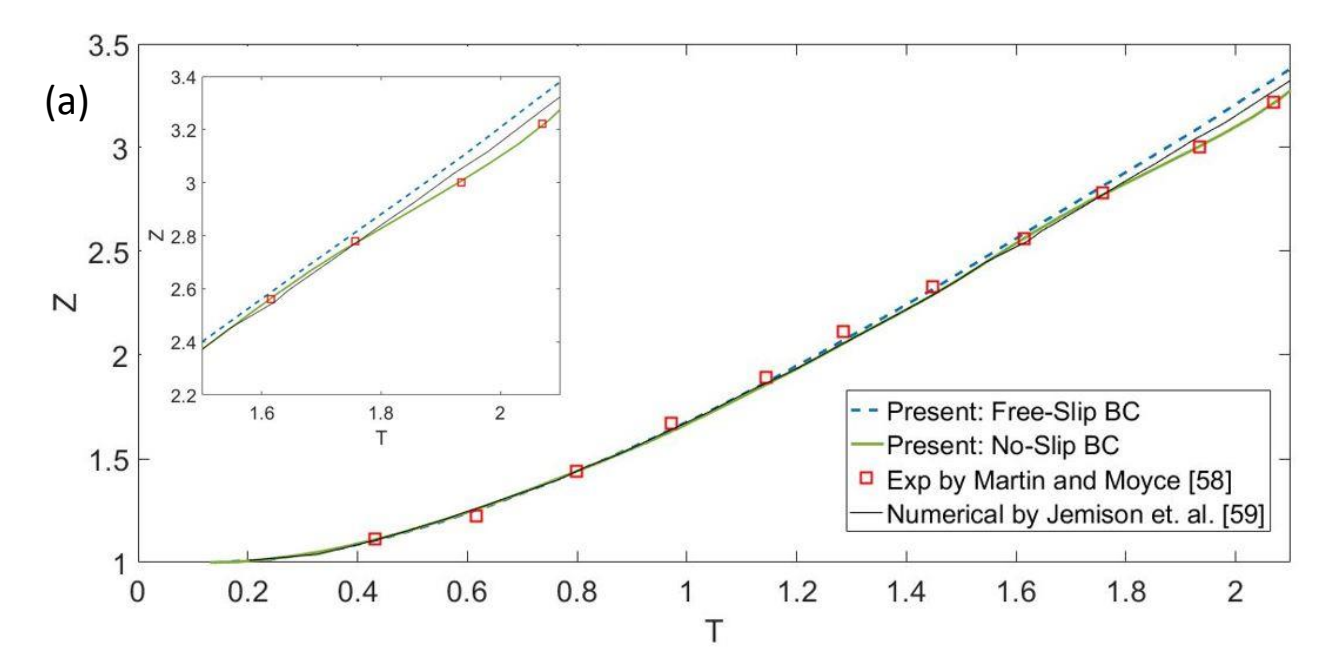
#### H. Dam Break/Collapsing Water Column

To further validate the capability of the present scheme to deal with large density ratio, we perform the dam break/collapsing water column case and compare our numerical result to the experimental measurements by Martin and Moyce [58] and to the numerical result by Jemison et. al. [59]. A water column is initially held steady. This initial configuration is unstable, and the water column will collapse, driven by gravity. Then the location of the front and the height of the water column at different instants were measured by Martin and Moyce [58] and we follow the notation in [58] that the location of the front is Z and the height of the water column is H. Both Z and H are scaled by the initial width of the water column a. The

computational domain is  $[4a \times 2a]$  and is discretized by 256×128 cells. A water column has an initial width and height of a, occupying  $[0, a] \times [0, a]$  of the domain, and is surrounded by air. The material properties of water and air are:

Air:  $\rho_{\rm air} = 1.204 {\rm kg/m^3}, \, \mu_{\rm air} = 1.78 \times 10^{-5} {\rm kg/(m \cdot s)}$  Water:  $\rho_{\rm water} = 998.207 {\rm kg/m^3}, \, \mu_{\rm water} = 1.002 \times 10^{-3} {\rm kg/(m \cdot s)}$  Surface Tension:  $\sigma = 7.28 \times 10^{-2} {\rm kg/s^2}$  Gravity:  $g_x = 0 {\rm m/s^2}, \, g_y = -9.8 {\rm m/s^2}.$ 

In this case, the density ratio is about 830 while the viscosity ratio is about 56. We use the scaling in [58], where a=2.25 inch (5.715cm) and the length scale, velocity scale and time scale are a,  $(|g_y|a)^{1/2}$  and  $(a/|g_y|)^{1/2}$ , respectively. We follow the same calibration in [58] that Z=1.44 when t=0.8 and H=1 when t=0. In addition, we perform two cases with the free-slip and the no-slip boundary conditions and  $\eta$  is set to be  $1.28\Delta y=0.01$  in both the cases. Quantitative comparisons are shown in Fig. 11.



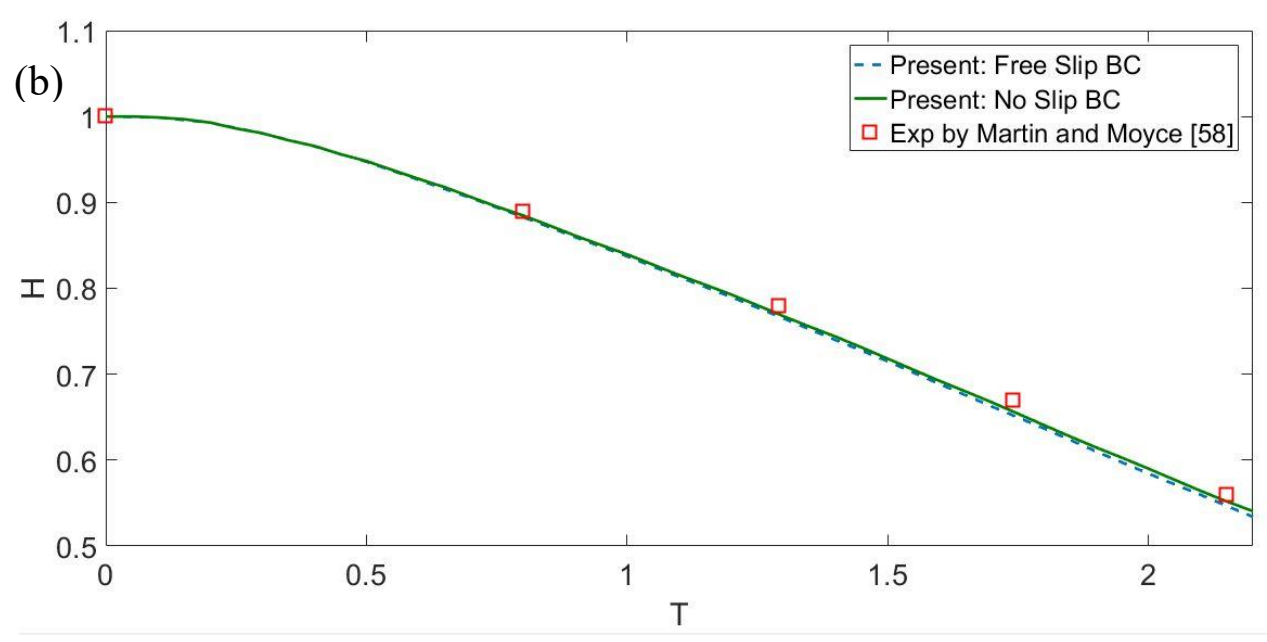


Fig. 11 Results of a dam break. (a) location of the front vs. time. (b) Height of the water column vs. time.

In Fig. 11 (a), initially, the large density ratio between the two fluids contributes to gravitational dominance so the numerical results are indistinguishable between the free-slip and no-slip boundary conditions. Both agree well with the experimental measurements. Later, however, discrepancies appear between these two cases. The curve of the free-slip case grows faster than the no-slip one. We can see that the no-slip case by the present scheme shares a similar growth rate to the experimental data and matches the measurements very well all the time, which is what we expected since no-slip boundary condition should better reproduce the experimental setup. Additionally, we also compared our result of the height of the water column with the experimental measurement in Fig 10 (b). Overall, both free-slip and no-slip boundary conditions match the measurement very well and no significant difference was observed between them although the no-slip one is a little closer to the measurement. These good agreements of our simulation with the experimental measurement indicate the capability of the present scheme, including the mixed Upwind/Central WENO scheme in section 3 and the efficient semi-implicit projection scheme in section 4, to handle large density ratio accurately.

We also compared our result with those in [59] by Jemison et. al. Their simulation solved the non-divergence form of the Navier-Stokes equations with no-slip boundary condition. The interface was captured by coupling level set and moment of fluid method with an elaborate interface reconstruction. The same manner of calibration as those in [58] is performed on the result in [59] so that the comparison is meaningful. Little difference between their result and ours can be observed at the beginning of the front propagation. However, discrepancies appear at later moments. The propagation of the front in [59] goes slower than our free-slip case because the no-slip boundary condition was imposed. It, however, goes faster than our no-slip case as well as than the experimental measurement in [58] although explicit interface reconstruction was conducted. The difference is not most likely rooted in the accuracy of interface capturing but in the significance of solving the divergence form of Navier-Stokes equations for long time simulations and large density ratio problems which have been also observed and reported in [24, 25].

# I. Rising Bubble with a Moving Contact Line

This final case includes several challenging factors, e.g., large density ratio, gravitation, surface tension and moving contact line. An air bubble is initially released with a zero velocity, surrounded by quiescent

water. The bubble rises due to buoyancy effects and gradually deforms. As the bubble rises further, it touches the top wall, resulting in a contact line between water, air, and wall. The contact line moves with spreading and shrinking of the bubble. The computational domain is  $[1 \times 1.5]$  and is discretized using  $100 \times 150$  cells. The no-slip and no-penetration boundary conditions are applied at all the domain boundaries. The material properties of water and air are

```
Air: \rho_{\rm air} = 1.204 \, {\rm kg/m^3}, \mu_{\rm air} = 1.78 \times 10^{-5} \, {\rm kg/(m \cdot s)}

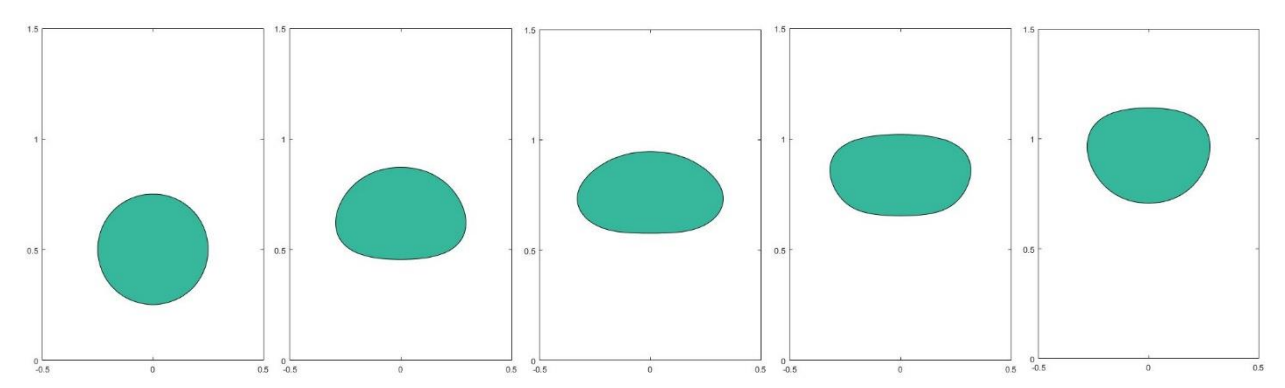
Water: \rho_{\rm water} = 998.207 \, {\rm kg/m^3}, \mu_{\rm water} = 1.002 \times 10^{-3} \, {\rm kg/(m \cdot s)}

Surface Tension: \sigma = 7.28 \times 10^{-2} \, {\rm kg/s^2}

Gravity: g_x = 0 \, {\rm m/s^2}, g_y = -9.8 \, {\rm m/s^2}.
```

The density ratio is about 830 while the viscosity ratio is about 56. The computations are performed for the dimensionless equations. The length scale is 0.01m, the characteristic density is the air density, and the gravitational scale is  $1 \text{m/s}^2$ . Based on the length, density, and gravitational scale, we can derive the dimensionless Eqs. (2.1 and 2.2). The bubble is initially at the centerline of the domain with radius 0.3 and the center of the bubble is 0.5 away from the bottom of the computational domain. The value of  $\eta$  is  $\Delta y = 0.01$ . The time step is  $2.5 \times 10^{-5}$  and the simulation is run for 100,000 time steps. Since there is no direct verification in this case, convergence tests are performed and are available in Appendix B for interested readers. Selected snapshots of the problem are shown in Fig. 12.

The bubble begins to rise because of buoyancy effects and deforms due to both horizontal spreading and vertical shrinking of the bubble. The deformation leads to a large curvature at the left and right sides of the bubble. The large curvature corresponds to a large surface energy, leading to strong surface forces. This energy is then redistributed along the interface in the form of a surface wave. We can observe the propagation and reflection of this surface wave along with the rising motion of the bubble. When the bubble touches the wall, some amount of water is trapped between the bubble and the top wall and multiple contact lines between water, air and solid wall are formed. Because of the inertia of the bubble, the contact lines begin to move along the top wall. This is the process of momentum transferring from *y* to *x*-direction since no momentum is allowed to cross the top wall. When the air bubble hits the lateral walls, a new surface wave is generated. This surface wave propagates and reflects between the centerline of the domain and the lateral walls while at the same time the amplitude is attenuated by viscosity.



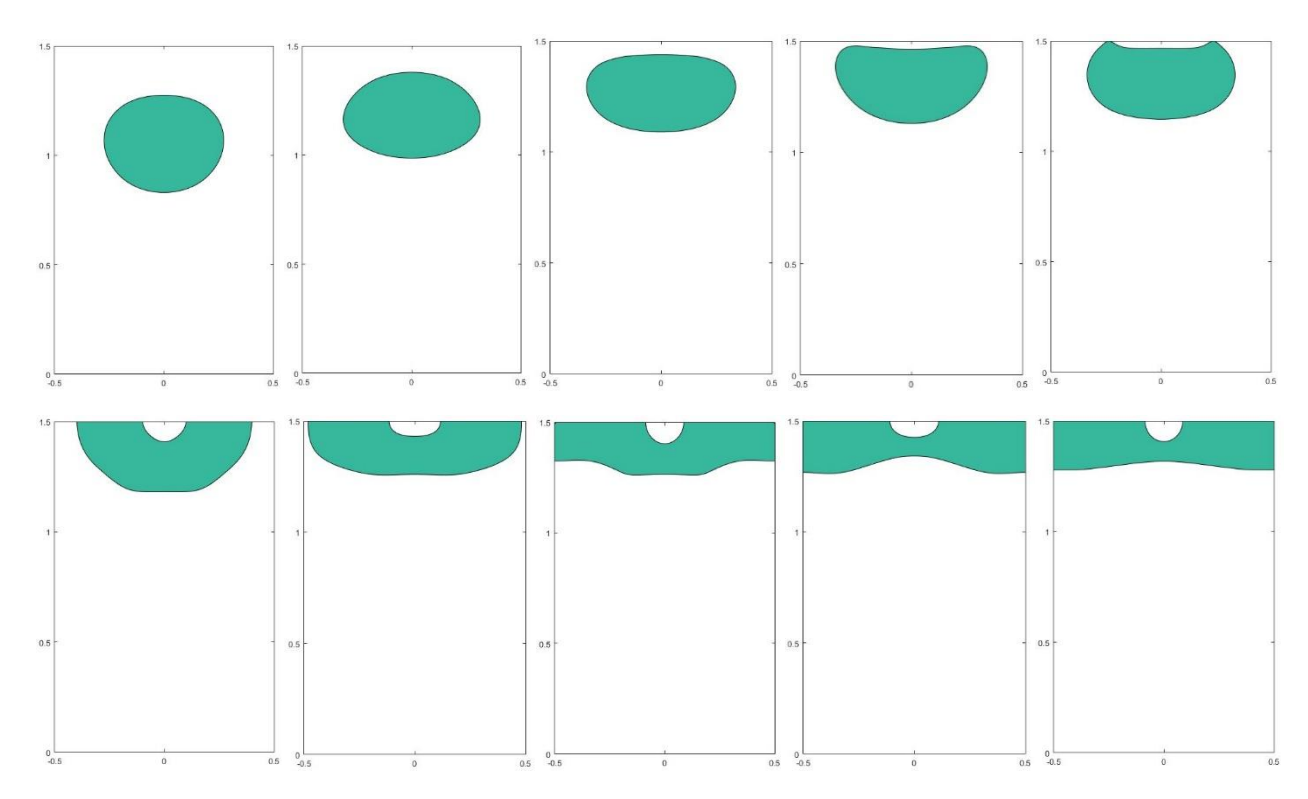


**Fig. 12** Results of rising bubble with moving contact line. From Left to Right and from Top to Bottom, *t*=0.025, 0.275, 0.4, 0.525, 0.65, 0.775, 0.9, 1.025, 1.15, 1.25, 1.425, 1.625, 1.725, 1.875, 2.4. Green: Air; White: Water

#### 6. Conclusion

In this paper, we developed a numerical scheme to accurately and efficiently solve the divergence form of the incompressible Navier-Stokes equations for two-phase flows. The difficulty of solving the divergence form in two-phase flows comes from the discontinuous nature of momentum across interfaces. To overcome this difficulty, we proposed a numerical scheme consisting of two parts: the mixed Upwind/Central WENO scheme, which discretizes the divergence convection term, and the efficient semi-implicit projection scheme with 2<sup>nd</sup>-order accurate for velocity, which decouples the entire two-phase Navier-Stokes equations. Compared to the recent progress on solving the divergence form of the Navier-Stokes equations in two/multi-phase flow, the proposed scheme has some preferable properties and advantages. It discretizes the equations on a fixed Eulerian grid, without any grid deformation or mapping, and it requires no explicit interface reconstruction, which makes it much easier to be implemented. Different from the existing schemes solving the divergence form, which are only compatible with a specific interface tracking/capturing method, e.g., Volume-of-Fluid method, our scheme is independent of the interface tracking/capturing methods, so it is flexible to couple with any popular methods, e.g., front tracking, level set, VOF or phase field method. This has been demonstrated by the results shown in the main text with the phase-field method to capture interfaces and in Appendix C with the Level-Set method.

Discretizing the divergence convection term is numerically challenging since momentum can change discontinuously/steeply across interfaces, especially when two fluids have large ratios of material properties. We proposed the mixed Upwind/Central WENO scheme to overcome the difficulty and numerical practice shows its ability to handle large density ratio of the order of  $(\rho_{\text{water}}/\rho_{\text{air}})$  accurately. Information from different stencils implies the locations of interfaces and the WENO construction procedure produce an appropriate combination of those stencils. Inspired by the idea of pressure stabilization, we construct an efficient semi-implicit projection scheme with formally  $2^{\text{nd}}$ -order accuracy for velocity to decouple the

entire two-phase system. The efficiency comes from the time-independent coefficient matrices resulting from the discretized algebraic system of the Navier-Stokes equations. Different from the pressure stabilization scheme, the velocity field in the present scheme is solenoidal, which is important to assure conservation for interface advection and reduction consistency. The formally 2<sup>nd</sup>-order temporal accuracy for velocity and reduction consistency of the projection scheme has been tested and confirmed by Taylor-Green vortex, lid-driven cavity flow, inviscid horizontal shear layer and a manufactured solution with variable density/viscosity. The effect of the viscosity ratio on spurious current is negligible with our scheme.

Several benchmark cases e.g., capillary wave, Rayleigh-Taylor instability and dam break/collapsing of the water column are performed to show the capability of the proposed scheme handling realistic two-phase problems with complex interface evolution and/or large density ratio of the order of  $(\rho_{\text{water}}/\rho_{\text{air}})$ . The interface is captured using the phase-field method and the convergence behavior of our scheme coupling with the phase-field method has been detailed discussed in the capillary wave case. Both quantitative and qualitative comparisons have been made and good agreements with the analytical solution, published numerical and/or experimental results are achieved in each case. The significance of solving the divergence form of the Navier-Stokes equations in large density ratio problems is observed in the dam break case, which is consistent with the observation in [24, 25]. Finally, the problem of a rising air bubble in water with moving contact lines is considered, where gravitation, surface tension, and viscosity are present and challenging circumstances of large density ratio and moving contact lines are included. Our results are able to reproduce the multiple physical behaviors of the problem.

## Acknowledgment

A.M. A. would like to acknowledge financial support from National Science Foundation (CBET-1705371).

G.L. would like to acknowledge the support from National Science Foundation (DMS- 1555072 and DMS- 1736364).

Z. H. would like to acknowledge financial support from Lynn Fellowship of Purdue University.

# **Appendix A: Mass Conservation**

Mass conservation is an important issue in two-phase flow simulations. It is the interface capturing method that is responsible for it. Although our scheme is compatible with any interface capturing/tracking methods, the phase-field method was used in the present work. We observed an excellent mass conservation in all our two-phase simulations, which we report in this appendix. We considered the mass as

$$M = \int_{\Omega} \frac{1+\phi}{2} d\Omega, \tag{A1}$$

where  $\phi$  is the phase filed function ranging from [-1,1] and  $\Omega$  is the whole computational domain. We compare the ratio of mass M to its initial value  $M_0$  in Fig. A1 to Fig. A4

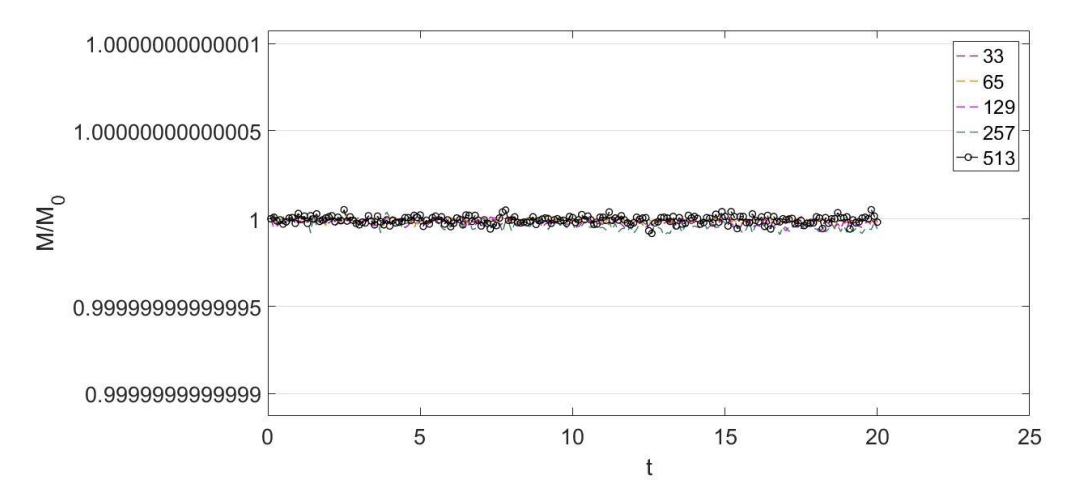


Fig. A1 Mass conservation of the capillary wave.

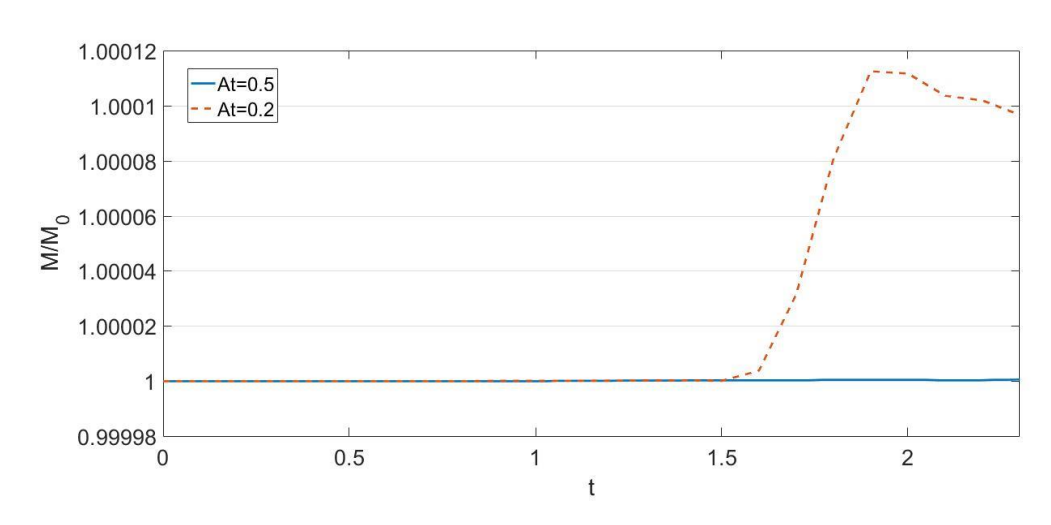


Fig. A2 Mass conservation of the Rayleigh-Taylor instability

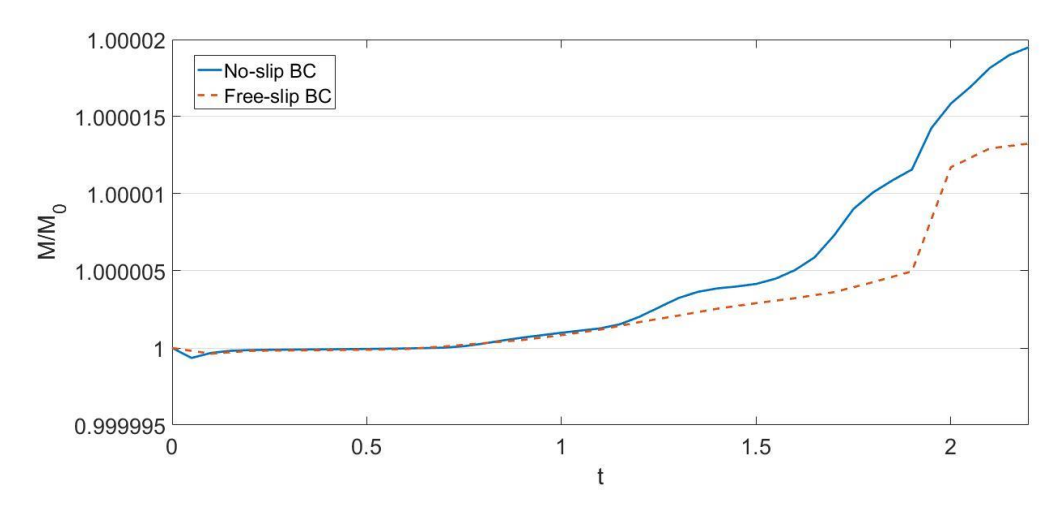


Fig. A3 Mass conservation of the dam break

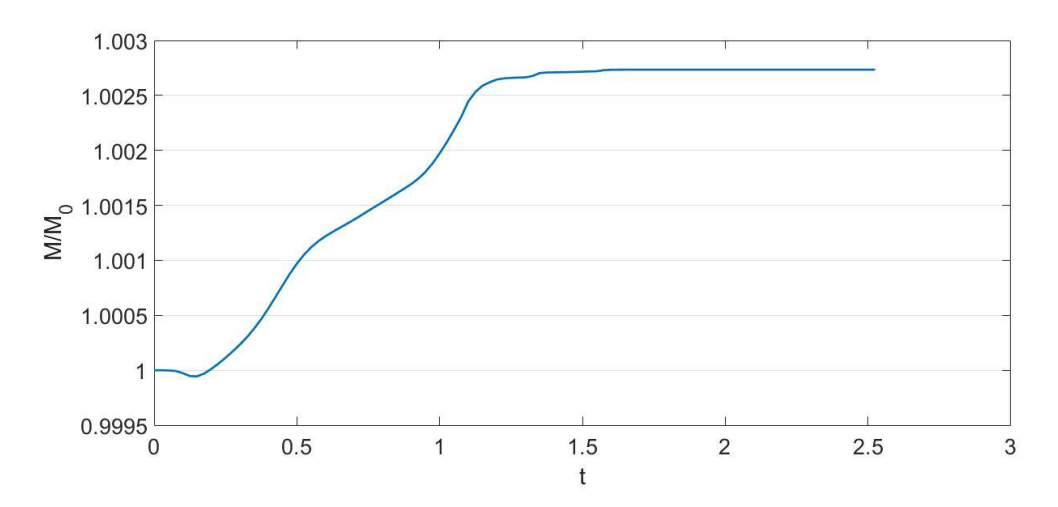


Fig. A4 Mass conservation of a rising bubble with contact lines

Fig. A1 to Fig. A4 show the mass conservation of the 4 two-phase cases we presented. The phase-field method has excellent mass conservation properties. The mass change in the capillary wave is almost zero. It is almost zero again in the Rayleigh-Taylor instability with At=0.5 while is less than 0.012% with At=0.2. In the dam break case, the variation of mass is less than 0.002% with both the no-slip and the free-slip boundary conditions. In the rising bubble case, the mass change is bounded by 0.3%. We note that the minor change of mass may result from setting the phase-field value to be 1 or -1 when its values are beyond interval [-1,1].

Based on the above-mentioned results, we conclude that the phase-field method has an excellent mass-conservation property.

# Appendix B: Convergence of a rising bubble with moving contact lines with respect to cell size and interface thickness

In this case, we consider the trajectory of the bubble, and its shape and location at t=0.9 with respect to different cell sizes  $h=\Delta x=\Delta y$  and interface thicknesses  $\eta$ . These results are shown in Fig.A5 and Fig.A6. The location of the bubble is defined as

$$y_{M} = \int_{\Omega} \frac{y(1+\phi)}{2} d\Omega / \int_{\Omega} \frac{1+\phi}{2} d\Omega. \tag{A2}$$

The convergence behavior is similar to what has been discussed in the capillary wave cases. All the results are converging when the cell size is refined and when the interface thickness is reduced. The differences between the solutions obtained with  $N_x = 100$  and those with  $N_x = 120$  are very small in the cases of  $\eta = 0.9\Delta x$ ,  $\Delta x$ ,  $1.2\Delta x$ , while obvious discrepancy is still observed in the case of  $\eta = 3\Delta x$ . Different interface thicknesses are explored by fixing  $N_x = 100$ , whose results are shown in Fig. A7. When reducing  $\eta$ , from  $10\Delta x$  to  $0.9\Delta x$ , the trajectory, shape and location of the bubble is converging. However, if the  $\eta$  continues to decrease, e.g.  $\eta = 0.8\Delta x$ , the intrinsic errors of the phase-field system appear. The result of  $\eta = 0.8\Delta x$  is close to that of  $\eta = 3\Delta x$ , which has not yet converged. The intrinsic errors keep increasing when  $\eta$  continues to decrease, and finally the interface is "trapped". Again, the convergence behavior in this case is consistent to the phase-field dynamics and its error analysis. It is also confirmed that the results shown in the main text, with  $N_x = 100$ ,  $\eta = \Delta x$  are acceptable.

We conclude that when using a phase-field method to capture the interface, an appropriate choice of  $\eta$  is important for successful two-phase simulations and careful validation should be performed.

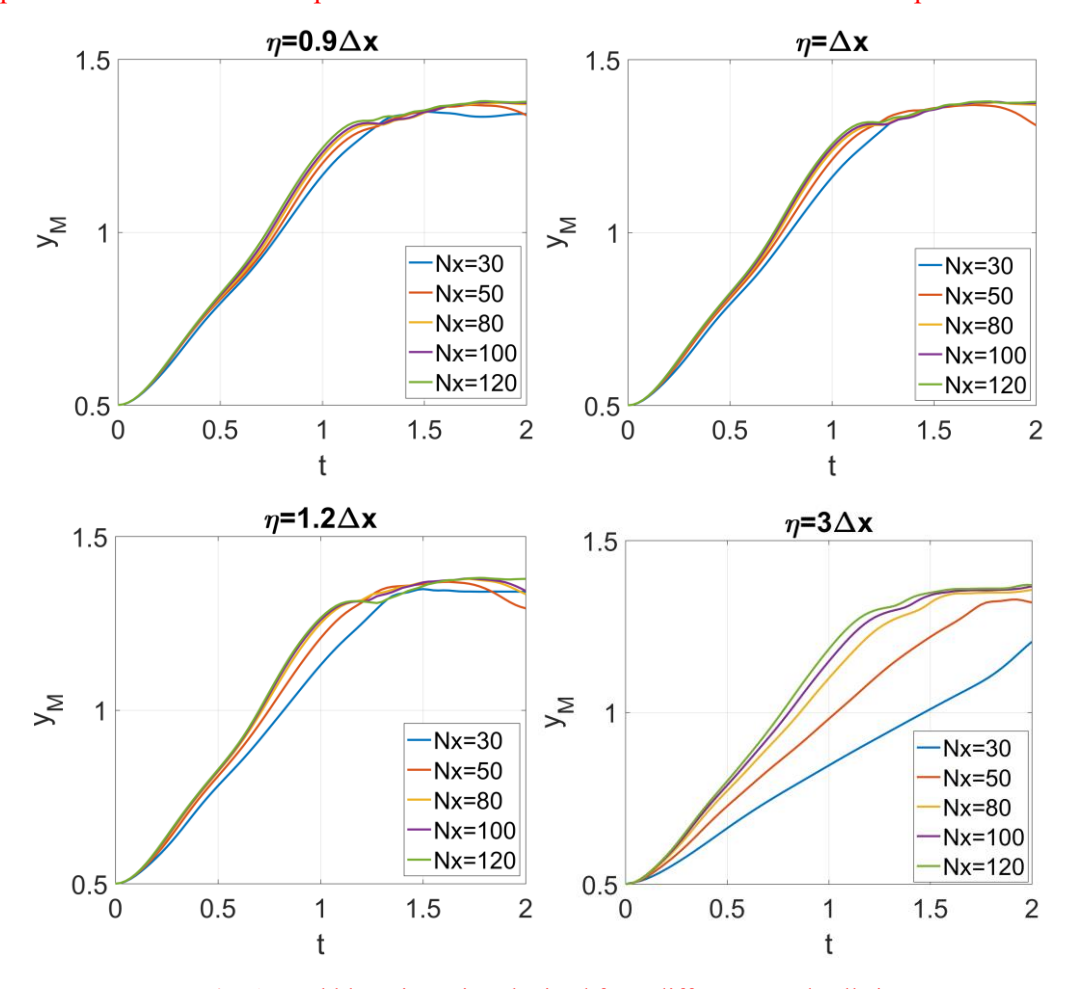


**Fig. A5** Bubble trajectories obtained from different  $\eta$  and cell sizes

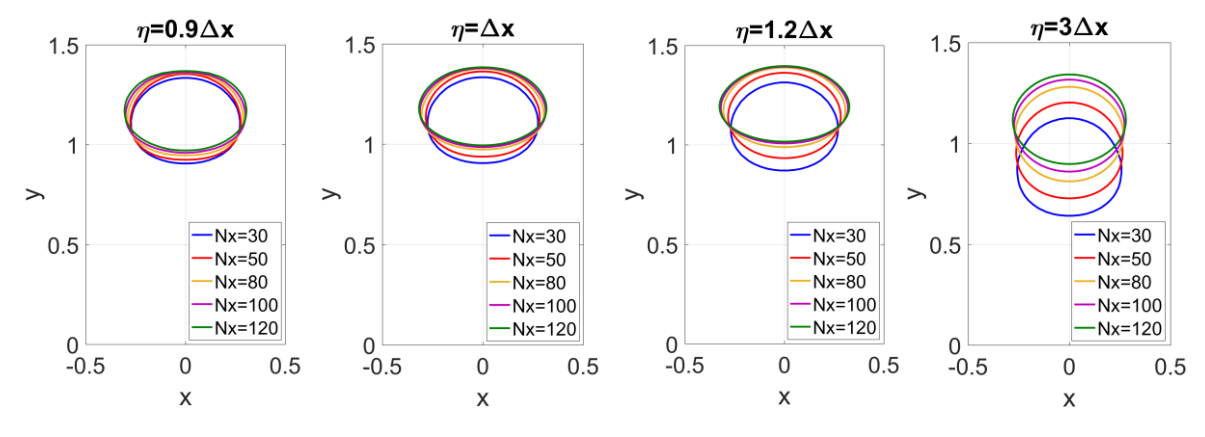


Fig. A6 Locations and shapes of bubbles at t = 0.9 with different  $\eta$  and cell sizes

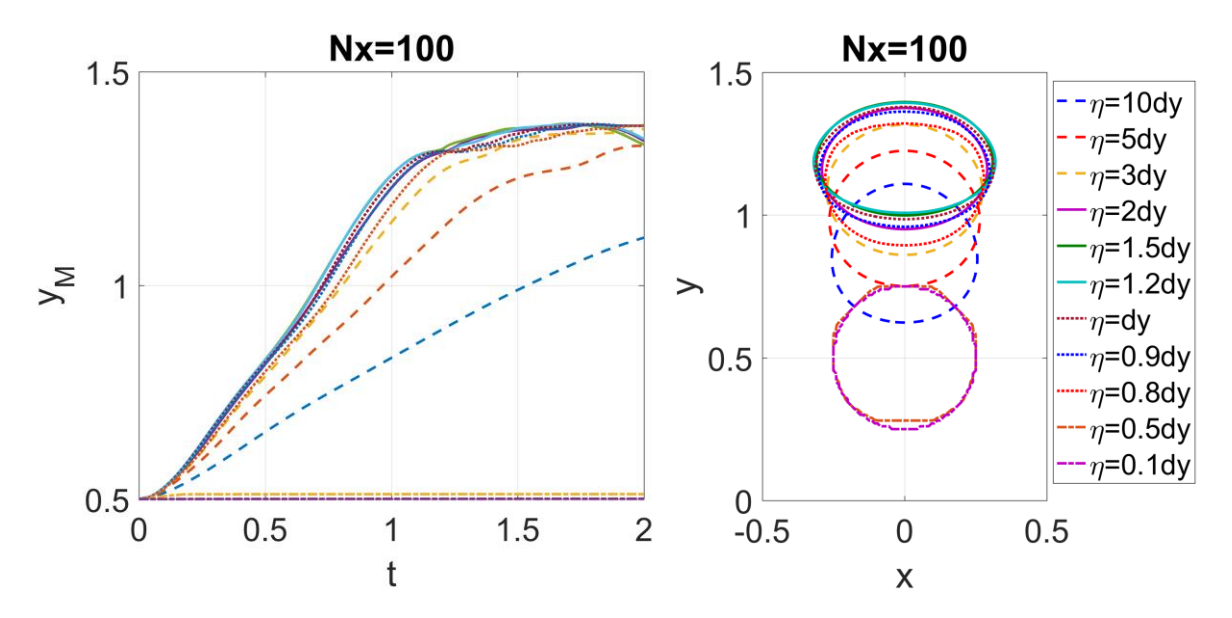


Fig. A7 Trajectories, locations and shapes of the bubbles at t = 0.9 with different  $\eta$  and fixed  $N_x = 100$ . Left: trajectories of the bubble; Right: Locations and shapes of the bubble

## **Appendix C: Coupling with the Level-Set Method**

The purpose of this section is to demonstrate the capability of our scheme easily coupling with different interface capturing/tracking methods. We replace the phase-field method with the Level-Set method [8] to capture interfaces for its popularity and simplicity of implementation. The interface is implicitly represented by the zero contours of a sign distance function  $\phi_{LS}$  and surface tension is modeled by a continuous surface force

$$\mathbf{f}_{S} = \sigma \kappa \nabla \widetilde{H}(\phi_{LS}), \tag{A3}$$

where  $\widetilde{H}$  is an approximated Heaviside function and is given in [8]. The  $\phi_{LS}$  is advected by

$$\frac{\partial \phi_{LS}^{ADV}}{\partial t} + \boldsymbol{u} \cdot \nabla \phi_{LS}^{ADV} = 0, \tag{A4}$$

and reinitialized by

$$\frac{\partial \phi_{LS}}{\partial \tau} + sign(\phi_{LS}^{ADV})(|\nabla \phi_{LS}| - 1) = 0, \tag{A5}$$

where  $\tau$  is pseudo time. The interface normal and curvature are defined as

$$\boldsymbol{n} = \frac{\nabla \phi_{LS}}{|\nabla \phi_{LS}|} \tag{A6}$$

and

$$\kappa = -\nabla \cdot \mathbf{n}. \tag{A7}$$

The 3<sup>rd</sup>-order TVD Runge-Kutta and 5<sup>th</sup>-order WENO schemes are used to solve the advection and reinitialization equations, and the central difference is used to compute interface normal and curvature. The more detailed explanation for the Level-Set method and its numerical discretization are referred to

[8, 51]. After solving the Level-Set function  $\phi_{LS}$ , the density field as well as the viscosity field are available from  $\rho = \rho_1 \tilde{H}(\phi_{LS}) + \rho_2 \left[1 - \tilde{H}(\phi_{LS})\right]$  and  $\mu = \mu_1 \tilde{H}(\phi_{LS}) + \mu_2 \left[1 - \tilde{H}(\phi_{LS})\right]$ . The continuous surface force  $f_s$  is also computable from  $\phi_{LS}$ . The rest is to input the  $\rho$ ,  $\mu$  and  $f_s$  into the scheme we proposed in the Section 3 and 4, and nothing needs changing. So, to couple our scheme with different interface capturing/tracking methods is very convenient and makes almost no effort.

For demonstration purpose, two cases are presented, which are the capillary wave and the Raleigh-Taylor instability. Fig. A8 to Fig. A10 show the numerical results obtained from the Level-Set method capturing the interface, continuous surface force modeling the surface effect, and the proposed scheme solving the two-phase Navier-Stokes system.

The grid-convergence results of the capillary wave can be observed in Fig. A8 and they converge correctly to the analytical solution [52].

The transient locations of the tips of bubbles going up and down by the Raleigh-Taylor instability with At=0.5 are shown in Fig. A9 and compared to the existing numerical results in [54-56]. Excellent agreements are achieved.

The flow patterns of the Rayleigh-Taylor instability with At=0.5 are shown in Fig. A10 and compared to the numerical results by Ding et.al [54]. Again, we achieve excellent agreement.

These tests demonstrate that our proposed scheme is flexible and convenient to couple with different interface capturing/tracking methods as long as material properties and surface tension model are provided.

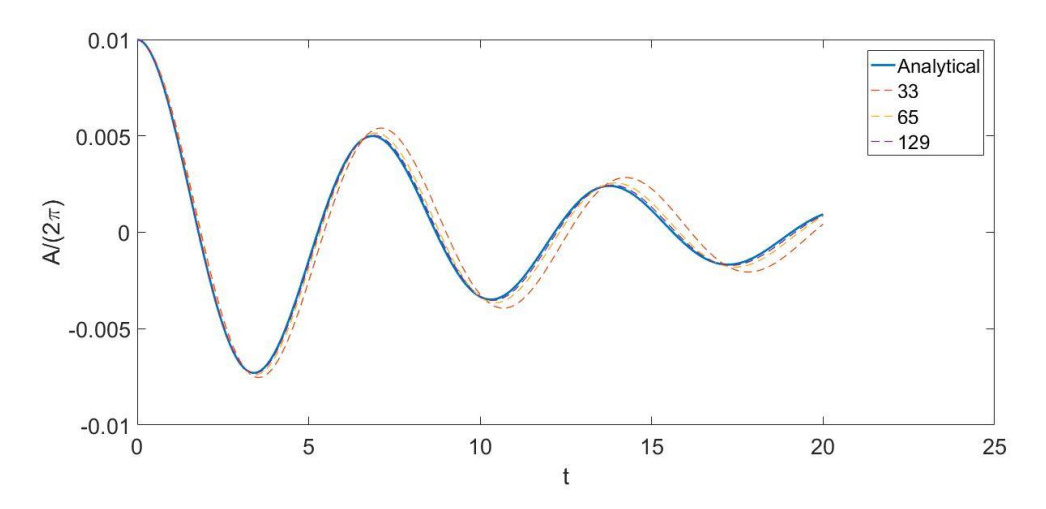
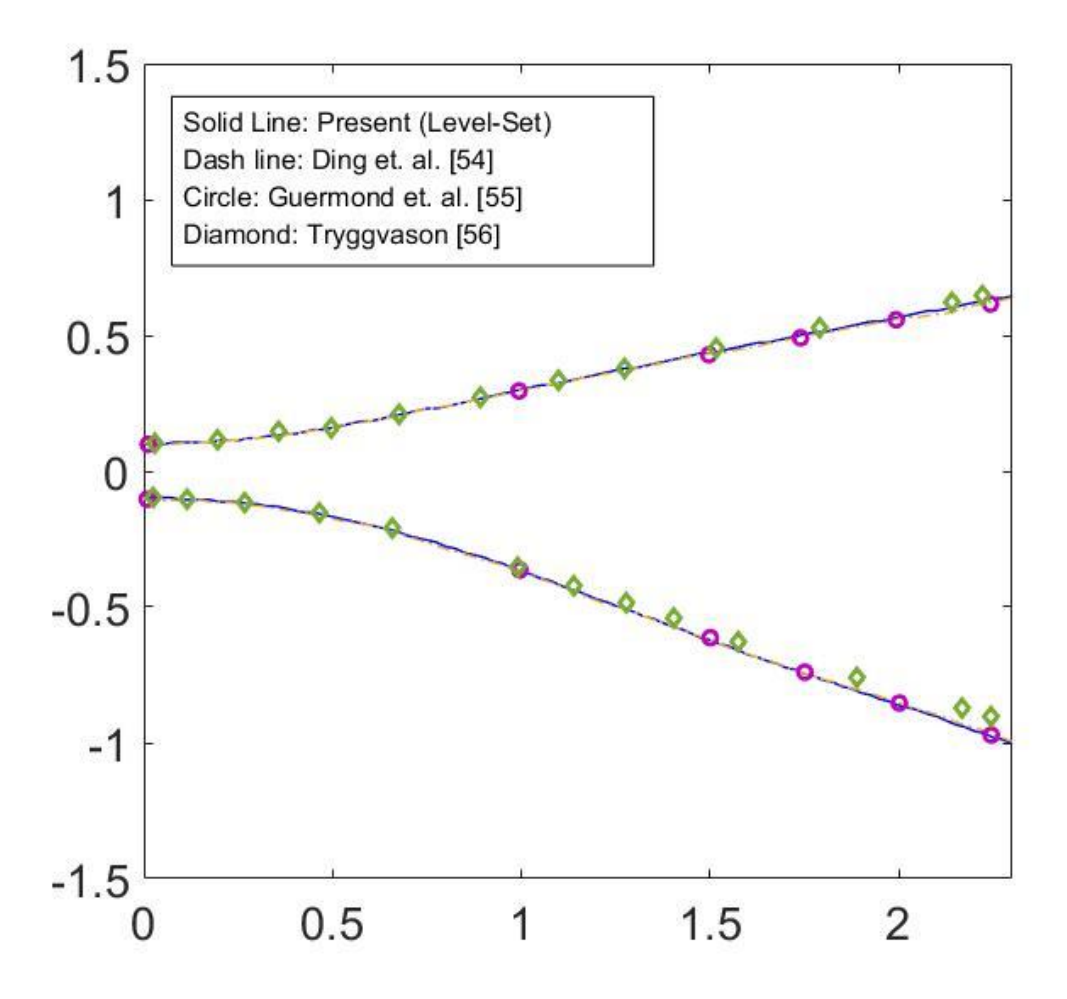
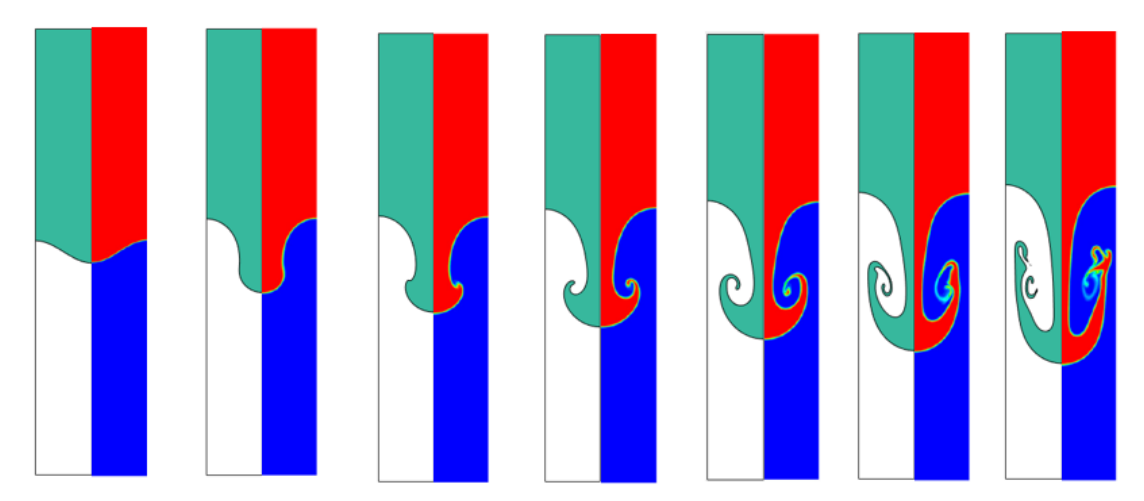


Fig. A8 Results of the capillary wave with the Level-Set method and continuous surface force



**Fig. A9** The transient locations of the tips of bubbles going up and down when *At*=0.5. Solid line: Present (Level-Set), Dash line: Ding et.al. [54], Circle: Guermond et. al. [55], Diamond: Tryggvason [56].



**Fig. A10** Flow patterns of the Rayleigh-Taylor instability with At=0.5 at t=0, 1, 1.25, 1.5, 1.75, 2, 2.25. Left Panels (green and white): Present with the Level-Set method, Right Panels (Blue and Red): Ding et. al. [54]. Green and Red: Denser fluid; White and Blue: Lighter fluid

#### Reference

- [1] Leal L. Advanced Transport Phenomena: Fluid Mechanics and Convective Transport Processes. Cambridge University Press; 2007.
- [2] Tryggvason G, Scardovelli R, Zaleski S. Direct Numerical Simulations of Gas-Liquid Multiphase Flows. Cambridge University Press; 2011.
- [3] Prosperetti A, Tryggvason G, editors. Computational methods for multiphase flow. Cambridge University Press; 2007.
- [4] Brackbill JU, Kothe DB and Zemach C. A continuum method for modeling surface tension. J. Comput. Phys. 1992; 100: 335–354.
- [5] Fedkiw RP, Aslam T, Merriman B, Osher S. A Non-oscillatory Eulerian Approach to Interfaces in Multimaterial Flows (the Ghost Fluid Method). J. Comput. Phys. 1999; 152: 457–492.
- [6] Lalanne B, Villegas LR, Tanguy S and Risso F. On the computation of viscous terms for incompressible two-phase flows with Level Set/Ghost Fluid Method. J. Comput. Phys. 2015; 301: 289–307.
- [7] Unverdi SO, Tryggvason G. A front-tracking method for viscous, incompressible, multi-fluid flows. J. Comput. Phys. 1992; 100: 25–37.
- [8] Sussman M, Smereka P, Osher S. A Level Set Approach for Computing Solutions to Incompressible Two-Phase Flow. J. Comput. Phys. 1994; 114: 146–159.
- [9] Olsson E and Kreiss G. A conservative level set method for two phase flow. J. Comput. Phys. 2005; 210: 225–246.
- [10] Olsson E, Kreiss G and Zahedi S. A conservative level set method for two phase flow II. J. Comput. Phys. 2007; 225: 785–807.
- [11] Chiodi R and Desjardins O. A reformulation of the conservative level set reinitialization equation for accurate and robust simulation of complex multiphase flows. J. Comput. Phys. 2017; 343: 186–200.
- [12] Hirt CW, Nichols BD. Volume of fluid (VOF) method for the dynamics of free boundaries. J. Comput. Phys. 1981; 39: 201–225.
- [13] Xie B and Xiao F. Toward efficient and accurate interface capturing on arbitrary hybrid unstructured grids: The THINC method with quadratic surface representation and Gaussian quadrature. J. Comput. Phys. 2017; 349: 415–4400.
- [14] Anderson DM, McFadden GB, Wheeler AA. Diffuse-interface methods in fluid mechanics. Annu. Rev. Fluid Mech. 1998; 30: 139-165.
- [15] Yue P, Feng JJ, Liu C, Shen J. A diffuse-interface method for simulating two-phase flows of complex fluids. J. Fluid Mech. 2004; 515: 293-317.
- [16] Gomez H, Hughes TJR, Nogueira X, Calo VM. Isogeometric analysis of the isothermal Navier-Stokes-Korteweg equations. Comput. Method Appl. M. 2010; 199: 1828-1840.

- [17] Dong S. Wall-bounded multiphase flows of N immiscible incompressible fluids: Consistency and contact-angle boundary condition. J. Comput. Phys. 2017; 338: 21–67.
- [18] Mirjalili S, Jain SS and Dodd MS. Interface-capturing methods for two-phase flows: An overview and recent developments. Center for Turbulence Research Annual Research Briefs 2017.
- [19] Francois M M, Cummins S J and Dendy ED, et. al. A balanced-force algorithm for continuous and sharp interfacial surface tension models within a volume tracking framework. J. Comput. Phys. 2006; 213: 141–173.
- [20] Akhlaghi Amiri HA and Hamouda AA. Evaluation of level set and phase field methods in modeling two phase flow with viscosity contrast through dual-permeability porous medium. International Journal of Multiphase Flow 2013; 52: 22-34.
- [21] Liu R, Wang D, Zhang X, Li Wang, Yu B. Comparison Study on the Performances of Finite Volume Method and Finite Difference Method. J. Appl. Math. 2013.
- [22] Fuster D, Agbaglah G, Josserand C, Popinet S, Zaleski S. Numerical simulation of droplets, bubbles and waves: state of the art. Fluid Dyn. Res. 2009; 41.
- [23] Rudman M. A Volume-Tracking Method for Incompressible Multifluid Flows with Large Density Variations. Int. J. Numer. Methods. Fluids 1998: 28:357-378.
- [24] Bussmann M, Kothe DB, Sicilian JM. Modeling High Density Ratio Incompressible Interfacial Flows. Proceedings of ADME Fluid Engineering Division Summer Meeting 2002-31125.
- [25] Raessi M, Pitsch H. Consistent mass and momentum transport for simulating incompressible interfacial flows with large density ratios using the level set method. Comput. Fluids 2012; 63: 70-81.
- [26] Chenadec VL, Pitsch H. A monotonicity preserving conservative sharp interface flow solver for high density ratio two-phase flows. J. Comput. Phys. 2013; 249: 185–203.
- [27] Owkes M, Desjardins O. A mass and momentum conserving unsplit semi-Lagrangian framework for simulating multiphase flows. J. Comput. Phys. 2017; 332: 21–46.
- [28] Chenadec VL, Pitsch H. A 3D Unsplit Forward/Backward Volume-of-Fluid Approach and Coupling to the Level Set Method. J. Comput. Phys. 2013; 233: 10–33.
- [29] Owkes M, Desjardins O. A computational framework for conservative, three-dimensional, unsplit, geometric transport with application to the volume-of-fluid (VOF) method. J. Comput. Phys. 2014; 270: 587–612.
- [30] Hussaini MY, Leer BV, Rosendale JV, editors. Upwind and High-Resolution Schemes. Springer 1997.
- [31] Jiang G-S, Shu C-W. Efficient Implementation of Weighted ENO Schemes. J. Comput. Phys. 1996; 126: 202–228.
- [32] Yang JY, Yang SC, Chen YN, Hsu CA. Implicit Weighted ENO Schemes for the Three-Dimensional Incompressible Navier-Stokes Equations. J. Comput. Phys. 1998; 146: 464–487.
- [33] Chen YN, Yang SH, Yang JY. Implicit Weighted Essentially Non-Oscillatory Schemes for the Incompressible Navier-Stokes Equations. Int. J. Numer. Meth. Fluids 1999; 31: 747–765.

- [34] Khurshid H, Hoffmann KA. Implementation of a WENO Scheme to the Incompressible Navier-Stokes Equations in Generalized Coordinate System. AIAA 2010: 40<sup>th</sup> Fluid Dynamics Conference and Exhibit.
- [35] Zhang J, Jackson TL. A high-order incompressible flow solver with WENO. J. Comput. Phys. 2009; 228: 2426–2442.
- [36] Harlow FH, Welch JE. Numerical Calculation of Time-Dependent Viscous Incompressible Flow of Fluid with Free Surface. Phys. Fluids 1965; 8: 2182-2189.
- [37] Guermond JL, Salgado Abner. A splitting method for incompressible flows with variable density based on a pressure Poisson equation. J Comput. Phys. 2009; 228: 2834–2846.
- [38] Liu C, Shen J, Yang X. Decoupled Energy Stable Schemes for a Phase-Field Model of Two-Phase Incompressible Flows with Variable Density. J. Sci. Comput. 2015; 62: 601-622.
- [39] Shen J, Yang X. Decoupled, Energy Stable Schemes for Phase-Field Models of Two-Phase Incompressible Flows. SIAM J. Numer. Anal. 2015; 53: 279-296.
- [40] Dong S, Shen J. A time-stepping scheme involving constant coefficient matrices for phase-field simulations of two-phase incompressible flows with large density ratios. J. Comput. Phys. 2012; 231: 5788–5804.
- [41] Dodd MS, Ferrante A. A fast pressure-correction method for incompressible two-fluid flows. J Comput. Phys. 2014; 273: 416–436.
- [42] Baraldi A, Dodd MS, Ferrante A. A mass-conserving volume-of-fluid method: Volume tracking and droplet surface-tension in incompressible isotropic turbulence. Computers & Fluids 2014; 96: 322-337.
- [43] Dodd MS, Ferrante A. On the interaction of Taylor length scale size droplets and isotropic turbulence. Journal of Fluid Mechanics 2016; 806: 356-412.
- [44] Badalassi VE, Ceniceros HD, Banerjee S. Computation of multiphase systems with phase field models. J. Comput. Phys. 2003; 190: 371–397.
- [45] Ferziger JH, Peric M. Computational Methods for Fluid Dynamics 3<sup>rd</sup> Edition. Springer; 2002.
- [46] Qiu J, Shu C-W. On the Construction, Comparison, and Local Characteristic Decomposition for High-Order Central WENO Schemes. J. Comput. Phys. 2002; 183: 187–209.
- [47] Bryson S, Levy Doron. High-Order Central WENO Schemes for Multidimensional Hamilton-Jacobi Equations. SIAM J. Numer. Anal. 2003; 41: 1339-1369;
- [48] Guermond JL, Minev P, Shen J. An overview of projection methods for incompressible flows. Comput. Methods Appl. Mech. Engrg 2006; 195: 6011-6045.
- [49] Ghia U, Chia KN, Shin CT. High-Re Solutions for Incompressible Flow Using the Navier-Stokes Equations and a Multigrid Method. J. Comput. Phys. 1982; 48: 387-411.
- [50] Bell JB, Colella P. A Second-Order Projection Method for the Incompressible Navier-Stokes Equations. J. Comput. Phys. 1989; 85: 257-283.
- [51] Herrmann M. A balanced force refined level set grid method for two-phase flows on unstructured flow solver grids. J. Comput. Phys. 2008; 227: 2674-2706.

- [52] Prosperetti A. Motion of two superposed viscous fluids. Phys. Fluids 1981; 24: 1217-1223.
- [53] Jacqmin D. Calculation of Two-Phase Navier-Stokes Flows Using Phase-Field Modeling. J. Comput. Phys. 1999; 155: 96-127.
- [54] Ding H, Spelt PDM, Shu C. Diffuse interface model for incompressible two-phase flows with large density ratios. J. Comput. Phys. 2007; 226: 2078-2095.
- [55] Guermond JL, Quartapelle L. A projection FEM for variable density incompressible flows. J. Comput. Phys. 2000; 165: 167-188.
- [56] Tryggvason G. Numerical simulations of the Rayleigh-Taylor instability. J. Comput. Phys. 1988; 75: 253-282.
- [57] Zhao L, Mao J, Bai X, Liu X, Li T, Williams JJR. Finite element implementation of an improved conservative level set method for two-phase flow. Computers & Fluids 2014; 100: 138-154.
- [58] Martin JC and Moyce WJ, An experimental study of the collapse of liquid columns on a rigid horizontal plane. Philosophical Transactions of the Royal Society of London, Series A 1952; 244: 312-324.
- [59] Jemison M, Loch E, Sussman M, Shashkov M, Arienti M, Ohta M, Wang Y. A Coupled Level Set-Moment of Fluid Method for Incompressible Two-Phase Flows. J Sci Comput 2013; 54: 454-491.